Journal of Computational Physics 229 (2010) 6047–6070

Contents lists available at ScienceDirect

Journal of Computational Physics

journal homepage: www.elsevier.com/locate/jcp

An algebraic variational multiscale–multigrid method for large-eddy simulation of turbulent variable-density flow at low Mach number

Volker Gravemeier [a,b,*], Wolfgang A. Wall [b]

[a] Emmy Noether Research Group "Computational Multiscale Methods for Turbulent Combustion", Technische Universität München, Boltzmannstr. 15, D-85748 Garching, Germany

[b] Institute for Computational Mechanics, Technische Universität München, Boltzmannstr. 15, D-85748 Garching, Germany

ARTICLE INFO

Article history:
Received 18 December 2009
Received in revised form 21 March 2010
Accepted 21 April 2010
Available online 29 April 2010

Keywords:
Turbulent variable-density flow
Large-eddy simulation
Finite element method
Variational multiscale method
Algebraic multigrid

ABSTRACT

An algebraic variational multiscale–multigrid method is proposed for large-eddy simulation of turbulent variable-density flow at low Mach number. Scale-separating operators generated by level-transfer operators from plain aggregation algebraic multigrid methods enable the application of modeling terms to selected scale groups (here, the smaller of the resolved scales) in a purely algebraic way. Thus, for scale separation, no additional discretization besides the basic one is required, in contrast to earlier approaches based on geometric multigrid methods. The proposed method is thoroughly validated via three numerical test cases of increasing complexity: a Rayleigh–Taylor instability, turbulent channel flow with a heated and a cooled wall, and turbulent flow past a backward-facing step with heating. Results obtained with the algebraic variational multiscale–multigrid method are compared to results obtained with residual-based variational multiscale methods as well as reference results from direct numerical simulation, experiments and LES published elsewhere. Particularly, mean and various second-order velocity and temperature results obtained for turbulent channel flow with a heated and a cooled wall indicate the higher prediction quality achievable when adding a small-scale subgrid-viscosity term within the algebraic multigrid framework instead of residual-based terms accounting for the subgrid-scale part of the non-linear convective term.

1. Introduction

Large-eddy simulation (LES) of turbulent flow aims at resolving the larger flow structures and modeling the effect of the smaller ones. The variational multiscale approach to LES (VMLES) as originally proposed in [1] and later addressed, e.g., in [2] further separates the resolved scales into larger and smaller ones; see, e.g., [3] for a review and several references therein. The other distinguishing feature of VMLES compared to the traditional LES approach is to be found in using variational projection instead of filtering for scale separation. The consideration of three scale groups (i.e., large resolved, small resolved, and unresolved scales) was already used before in the context of the dynamic modeling procedure proposed in [4]. It is based on a scale-similarity hypothesis (with respect to smaller resolved and unresolved scales) earlier exploited in the scale-similarity model [5].

LES has successfully been applied to both incompressible (see, e.g., [6]) and compressible (see, e.g., [7]) turbulent flow. More rarely, applications of LES to turbulent variable-density flow at low Mach number are encountered in literature. This

* Corresponding author at: Emmy Noether Research Group "Computational Multiscale Methods for Turbulent Combustion", Technische Universität München, Boltzmannstr. 15, D-85748 Garching, Germany. Tel.: +49 89 28915245; fax: +49 89 28915301.
E-mail addresses: vgravem@lnm.mw.tum.de (V. Gravemeier), wall@lnm.mw.tum.de (W.A. Wall).

0021-9991/$ - see front matter © 2010 Elsevier Inc. All rights reserved.
doi:10.1016/j.jcp.2010.04.036

is despite the importance of the problems mathematically described by this set of equations. In particular, problems of combustion are usually mathematically described by a variable-density formulation of the Navier–Stokes equations for low-speed flows, see, e.g., [8,9]. A rigorous derivation of the equation system at low Mach number with a view on combustion problems can be found, e.g., in [10]. Methods for LES of reactive and/or non-reactive turbulent low-Mach-number flow are proposed, for instance, based on finite-volume approaches in [11–15] and based on a finite-difference approach in [16]. In most studies, the version of the dynamic Smagorinsky model in [17], which extended the original proposal in [4] for incompressible flow to the compressible case and scalar transport, is used as subgrid-scale model. For the scalar transport equation, a subgrid diffusivity is used which is defined by the ratio of the subgrid viscosity used in the momentum equation and a turbulent Prandtl number as earlier proposed by Erlebacher et al. see, e.g., [18]. An overview on traditional subgrid-scale models for turbulent compressible flows can also be found in [19].

All of the aforementioned LES studies were used within finite-volume- or finite-difference-based computational environments. Finite element methods (FEM) for non-reactive low Mach number flow using inf-sup stable elements are described, e.g., in [20–22]. Residual-based variational multiscale methods or stabilized FEM were recently proposed for such problems in [23,24]. Stabilized FEM for reactive flow had been addressed before by Hauke and Valiño (see [25]), by Shadid and various co-workers at Sandia National Laboratories (see, e.g., [26], and references therein) as well as by Braack and co-workers (see, e.g., [27], and references therein). However, all aforementioned publications merely addressed *laminar* low-Mach-number flow situations. In particular, to the best of our knowledge, there have not yet been any studies on FEM for (non-reactive) variable-density *turbulent* flows at low Mach number published.

In a predecessor study to the present one, [28], we developed a residual-based variational multiscale method for low-Mach number flow suitable for simulating laminar via transitional to turbulent flow regimes. That approach extends the respective method proposed in [29] for turbulent incompressible flow to the low-Mach number case and is based on the general framework of the variational multiscale method (see, e.g., [30]). It has similarities with the methods used in [23,24]. However, we already observed considerably improved results in the context of turbulent incompressible flow when including a small-scale subgrid-viscosity model in the sense of a VMLES. The present work will show that such an improvement is also achievable for variable-density flow by developing a formulation which features such a small-scale subgrid-viscosity model in the sense of a VMLES. For a method to be used for a VMLES, the crucial aspect is the way large and small resolved scales are separated.

The framework of an algebraic variational multiscale–multigrid method (AVM^3) was originally proposed in [31] and applied to convection-dominated convection–diffusion problems. It was further developed and extended for application to turbulent flow in the form of LES in [32]. The scale separation is based on level-transfer operators arising in plain aggregation algebraic multigrid (PA-AMG); see, e.g., [33]. Though conceptually different, PA-AMG is closely related to volume-agglomeration multigrid methods (see, e.g., [34,35]), which were preferably developed for finite-volume discretizations of hyperbolic problems. A scale separation inspired by a volume-agglomeration method as proposed in [34] was used in [36] within a VMLES. Geometric multigrid approaches to LES had already been proposed in [37] and later in [38]; see also the recent review in [39]. Those methods were not derived using the framework of the VMLES. A geometric multigrid approach to VMLES was later developed in [40]. Compared to those geometric multigrid procedures, the present algebraic multigrid method obviates the often challenging generation of additional meshes besides the basic one.

The present study proposes the AVM^3 for LES of turbulent variable-density flow at low Mach number. The study is organized as follows. In Section 2, the variable-density equation system at low Mach number in two alternative formulations is given. Afterwards, a residual-based variational multiscale formulation is derived in Section 3. This section serves two purposes. On the one hand, the reader is familiarized with the method the AVM^3 is compared to. On the other hand, some of the terms introduced in the residual-based variational multiscale formulation are also employed for the AVM^3, which is then provided in Section 5, after a brief presentation of the time-integration and solution procedures in Section 4. The AVM^3 is then validated for three numerical examples, a Rayleigh–Taylor instability, turbulent channel flow with a heated and a cooled wall and turbulent flow past a backward-facing step with heating, in Section 6. Results obtained with the AVM^3 are compared to results obtained with residual-based variational multiscale methods as well as reference results from direct numerical simulation (DNS), experiments and LES published elsewhere. Conclusions from this study are drawn in Section 7.

2. Two formulations of the variable-density equations at low Mach number

2.1. Temperature formulation

Conservation equations for mass, momentum and energy in the domain Ω are given in convective form as

$$\frac{\partial \rho}{\partial t} + \nabla \cdot (\rho \mathbf{u}) = 0, \tag{1}$$

$$\rho \frac{\partial \mathbf{u}}{\partial t} + \rho \mathbf{u} \cdot \nabla \mathbf{u} + \nabla p_{\mathrm{hyd}} - \nabla \cdot (2\mu \varepsilon'(\mathbf{u})) = \rho \mathbf{g}, \tag{2}$$

$$\rho \frac{\partial T}{\partial t} + \rho \mathbf{u} \cdot \nabla T - \nabla \cdot \left(\frac{\lambda}{c_p} \nabla T \right) = \frac{1}{c_p} \left[\frac{dp_{\mathrm{the}}}{dt} + Q \right], \tag{3}$$

where ρ denotes the density, $\mathbf{u}$ is the velocity, p_{hyd} is the hydrodynamic pressure, μ is the viscosity, $\varepsilon'(\mathbf{u}) = \varepsilon(\mathbf{u}) - \frac{1}{3}(\nabla \cdot \mathbf{u})\mathbf{I}$, with the rate-of-deformation tensor $\varepsilon(\mathbf{u}) = \frac{1}{2}(\nabla\mathbf{u} + (\nabla\mathbf{u}^T))$, $\mathbf{I}$ is the identity tensor, $\mathbf{g}$ is the gravity force vector, T is the temperature, c_p is the specific heat capacity at constant pressure (assumed constant), λ the thermal conductivity, p_{the} is the thermodynamic pressure and Q is a potential heat source. Properties μ and λ are assumed to vary with T according to Sutherland's law:

$$\mu = \left(\frac{T}{T_{\text{ref}}}\right)^{\frac{3}{2}}\left(\frac{T_{\text{ref}} + S}{T + S}\right)\mu_{\text{ref}}, \quad \lambda = \frac{c_p}{\text{Pr}}\mu,$$

using a reference temperature T_{ref}, a reference viscosity μ_{ref}, the Sutherland temperature S, and the Prandtl number $\text{Pr} = \frac{c_p\mu}{\lambda}$. Note that energy conservation (3) is expressed in terms of temperature. Additionally, the equation of state for an ideal gas,

$$\rho = \frac{p_{\text{the}}}{RT} \tag{4}$$

is assumed based on the gas constant R. Using (4), the mass-conservation Eq. (1) may be reformulated as

$$\nabla \cdot \mathbf{u} = \frac{1}{T}\left(\frac{\partial T}{\partial t} + \mathbf{u} \cdot \nabla T\right) - \frac{1}{p_{\text{the}}}\frac{dp_{\text{the}}}{dt}. \tag{5}$$

As demonstrated in [28], by way of adding specific subgrid-scale terms, momentum–conservation properties may be achieved even when starting from a convective form. The evidence given in [28] used the proof provided in [41] for the incompressible Navier–Stokes equations as the starting point and further developed it for the present variable-density Navier–Stokes equations.

Initial conditions are prescribed for $\mathbf{u}$ and T:

$$\mathbf{u}(\mathbf{x}, t = 0) = \mathbf{u}_0(\mathbf{x}), \quad T(\mathbf{x}, t = 0) = T_0(\mathbf{x}).$$

Dirichlet and Neumann boundary conditions for (2),

$$\mathbf{u} = \mathbf{u}_{\text{D}} \quad \text{on } \Gamma_{\text{D,u}},$$
$$\left(-p_{\text{hyd}}\mathbf{I} + 2\mu\varepsilon'(\mathbf{u})\right) \cdot \mathbf{n} = \mathbf{h}_{\text{u}} \quad \text{on } \Gamma_{\text{N,u}}$$

and for (3),

$$T = T_{\text{D}} \quad \text{on } \Gamma_{\text{D,T}},$$
$$\frac{\lambda}{c_p}\nabla T \cdot \mathbf{n} = h_{\text{T}} \quad \text{on } \Gamma_{\text{N,T}},$$

are also prescribed. It is assumed that $\Gamma_{\text{D}} \cap \Gamma_{\text{N}} = \emptyset$, $\Gamma_{\text{D}} \cup \Gamma_{\text{N}} = \Gamma$ for each equation, and $\mathbf{n}$ denotes the outer unit normal on the boundary.

For two of the numerical examples considered below, turbulent channel flow and turbulent flow past a backward-facing step, two different situations need to be distinguished with respect to determining the thermodynamic pressure. On the one hand, the configuration of the backward-facing step represents an open system due to the Neumann outflow boundary (i.e., $\Gamma_{\text{N,u}} \neq \varnothing$), which determines the (constant) thermodynamic pressure in this case. On the other hand, the channel is a closed system (i.e., $\Gamma_{\text{N,u}} = \varnothing$). The total mass remains constant over time in the channel domain. Thus, p_{the} may be obtained at each time subject to an integral form of (4),

$$p_{\text{the}} = R\frac{\int_\Omega \rho\, d\Omega}{\int_\Omega \frac{1}{T}\, d\Omega} = R\frac{\int_\Omega \rho_0\, d\Omega}{\int_\Omega \frac{1}{T}\, d\Omega} = \frac{RM_0}{\int_\Omega \frac{1}{T}\, d\Omega},$$

where M_0 denotes the initial total mass in Ω.

2.2. Mixture-fraction formulation

As an alternative equation system replacing (3)–(5), a mixture-fraction formulation will be considered for the first numerical example below, as was also done in [16]. Mixture fraction is an important value frequently used in non-premixed combustion; see, e.g., [8,9] for details. Eq. (3) is replaced by

$$\rho\frac{\partial Z}{\partial t} + \rho\mathbf{u} \cdot \nabla Z - \nabla \cdot (\rho D_Z \nabla Z) = 0, \tag{6}$$

where Z denotes the mixture fraction and D_Z a (kinematic) diffusivity. Furthermore, an equation of state for two miscible fluids,

$$\rho = \frac{1}{aZ + b}, \tag{7}$$

as used in [16] is defined. For the present formulation, using (7), the mass-conservation Eq. (1) may be reformulated as

$$\nabla \cdot \mathbf{u} = a\rho\left(\frac{\partial Z}{\partial t} + \mathbf{u} \cdot \nabla Z\right). \tag{8}$$

However, in order not to unneccessarily elongate the presentation in the upcoming sections, only the first alternative using Eqs. (3)–(5) will be taken into account. The derivation of the alternative formulations is straightforward.

3. Residual-based variational multiscale formulation

To obtain a variational formulation of the variable-density equations at low Mach number, appropriate solution function spaces $\mathcal{S}_{\{p,\mathbf{u},T\}}$ for p_{hyd},$\mathbf{u}$ and T as well as weighting function spaces $\mathcal{V}_{\{p,\mathbf{u},T\}}$ for the respective weighting functions q, $\mathbf{v}$ and w are assumed. The variational formulation is given as follows: find $p_{\text{hyd}} \in \mathcal{S}_p, \mathbf{u} \in \mathcal{S}_{\mathbf{u}}$ and $T \in \mathcal{S}_T$ such that

$$(q, \nabla \cdot \mathbf{u}) = \left(q, \frac{1}{T}\left(\frac{\partial T}{\partial t} + \mathbf{u} \cdot \nabla T\right) - \frac{1}{p_{\text{the}}}\frac{dp_{\text{the}}}{dt}\right) \quad \forall q \in \mathcal{V}_p, \tag{9}$$

$$\left(\mathbf{v}, \rho\frac{\partial \mathbf{u}}{\partial t}\right) + (\mathbf{v}, \rho\mathbf{u} \cdot \nabla\mathbf{u}) - (\nabla \cdot \mathbf{v}, p_{\text{hyd}}) + (\varepsilon(\mathbf{v}), 2\mu\varepsilon'(\mathbf{u})) = (\mathbf{v}, \rho\mathbf{g}) + (\mathbf{v}, \mathbf{h}_{\text{u}})_{\Gamma_{\text{N,u}}} \quad \forall \mathbf{v} \in \mathcal{V}_{\mathbf{u}}, \tag{10}$$

$$\left(w, \rho\frac{\partial T}{\partial t}\right) + (w, \rho\mathbf{u} \cdot \nabla T) + \left(\nabla w, \frac{\lambda}{c_p}\nabla T\right) = \left(w, \frac{1}{c_p}\left[\frac{dp_{\text{the}}}{dt} + Q\right]\right) + (w, h_T)_{\Gamma_{\text{N,T}}} \quad \forall w \in \mathcal{V}_T, \tag{11}$$

where $(\cdot,\cdot) = (\cdot,\cdot)_{\Omega}$ and $(\cdot,\cdot)_{\Gamma_{\text{N}}}$ denote the usual L_2-inner product on Ω and Γ_{N}, respectively.

A variational projection for separating resolved and unresolved scales within an FEM is assumed here. Hence, hydrodynamic pressure, velocity and temperature fields are decomposed via variational projection into resolved and unresolved (or subgrid-scale) parts as

$$p_{\text{hyd}} = p^h_{\text{hyd}} + \hat{p}_{\text{hyd}}, \quad \mathbf{u} = \mathbf{u}^h + \hat{\mathbf{u}}, \quad T = T^h + \widehat{T}, \tag{12}$$

where h denotes the characteristic length scale of the discretization. The subgrid-scale parts of hydrodynamic pressure, velocity and temperature field are approximated in an elementwise manner based on the resolved-scale parts. Hence, in each element, the subgrid-scale parts are given as

$$\hat{p}_{\text{hyd}} = -\tau_{\text{C}}\mathcal{R}^h_{\text{C}}, \quad \hat{\mathbf{u}} = -\tau_{\text{M}}\mathcal{R}^h_{\text{M}}, \quad \widehat{T} = -\tau_{\text{E}}\mathcal{R}^h_{\text{E}}, \tag{13}$$

using respective stabilization parameters τ, which will be defined below. The discrete residuals of mass, momentum and energy conservation read

$$\mathcal{R}^h_{\text{C}} = \nabla \cdot \mathbf{u}^h - \frac{1}{T^h}\left(\frac{\partial T^h}{\partial t} + \mathbf{u}^h \cdot \nabla T^h\right) + \frac{1}{p^h_{\text{the}}}\frac{dp^h_{\text{the}}}{dt},$$

$$\mathcal{R}^h_{\text{M}} = \rho^h\frac{\partial \mathbf{u}^h}{\partial t} + \rho^h\mathbf{u}^h \cdot \nabla\mathbf{u}^h + \nabla p^h_{\text{hyd}} - \nabla \cdot (2\mu^h\varepsilon'(\mathbf{u}^h)) - \rho^h\mathbf{g},$$

$$\mathcal{R}^h_{\text{E}} = \rho^h\frac{\partial T^h}{\partial t} + \rho^h\mathbf{u}^h \cdot \nabla T^h - \nabla \cdot \left(\frac{\lambda^h}{c_p}\nabla T^h\right) - \frac{1}{c_p}\left[\frac{dp^h_{\text{the}}}{dt} + Q\right].$$

The residual-based variational multiscale FE formulation is obtained by introducing decomposition (12) and approximation (13) into the variational formulation (9)–(11) and proceeding as described in [28]: find $p^h_{\text{hyd}} \in \mathcal{S}^h_p, \mathbf{u}^h \in \mathcal{S}^h_{\mathbf{u}}$ and $T^h \in \mathcal{S}^h_T$ such that

$$(q^h, \nabla \cdot \mathbf{u}^h) + (\nabla q^h, \tau_{\text{M}}\mathcal{R}^h_{\text{M}}) = \left(q^h, \frac{1}{T^h}\left(\frac{\partial T^h}{\partial t} + \mathbf{u}^h \cdot \nabla T^h\right) - \frac{1}{p^h_{\text{the}}}\frac{dp^h_{\text{the}}}{dt}\right) \quad \forall q^h \in \mathcal{V}^h_p, \tag{14}$$

$$\begin{aligned}
&\left(\mathbf{v}^h, \rho^h\frac{\partial \mathbf{u}^h}{\partial t}\right) + (\mathbf{v}^h, \rho^h\mathbf{u}^h \cdot \nabla\mathbf{u}^h) - \left(\nabla \cdot \mathbf{v}^h, p^h_{\text{hyd}}\right) + (\varepsilon(\mathbf{v}^h), 2\mu^h\varepsilon'(\mathbf{u}^h)) + (\nabla \cdot \mathbf{v}^h, \tau_{\text{C}}\mathcal{R}^h_{\text{C}}) + (\rho^h\mathbf{u}^h \cdot \nabla\mathbf{v}^h, \tau_{\text{M}}\mathcal{R}^h_{\text{M}}) \\
&\quad - (\mathbf{v}^h, \rho^h\tau_{\text{M}}\mathcal{R}^h_{\text{M}} \cdot \nabla\mathbf{u}^h) - (\rho^h\tau_{\text{M}}\mathcal{R}^h_{\text{M}} \cdot \nabla\mathbf{v}^h, \tau_{\text{M}}\mathcal{R}^h_{\text{M}}) \\
&\quad = (\mathbf{v}^h, \rho^h\mathbf{g}) + (\mathbf{v}^h, \mathbf{h}_{\mathbf{u}})_{\Gamma_{\text{N,u}}} \quad \forall \mathbf{v}^h \in \mathcal{V}^h_{\mathbf{u}},
\end{aligned} \tag{15}$$

$$\begin{aligned}
&\left(w^h, \rho^h\frac{\partial T^h}{\partial t}\right) + \left(w^h, \rho^h\mathbf{u}^h \cdot \nabla T^h\right) + \left(\nabla w^h, \frac{\lambda^h}{c_p}\nabla T^h\right) + (\rho^h\mathbf{u}^h \cdot \nabla w^h, \tau_{\text{E}}\mathcal{R}^h_{\text{E}}) - \left(w^h, \rho^h\tau_{\text{M}}\mathcal{R}^h_{\text{M}} \cdot \nabla T^h\right) \\
&\quad - (\rho^h\tau_{\text{M}}\mathcal{R}^h_{\text{M}} \cdot \nabla w^h, \tau_{\text{E}}\mathcal{R}^h_{\text{E}}) \\
&\quad = \left(w^h, \frac{1}{c_p}\left[\frac{dp^h_{\text{the}}}{dt} + Q\right]\right) + (w^h, h_T)_{\Gamma_{\text{N,T}}} \quad \forall w^h \in \mathcal{V}^h_T
\end{aligned} \tag{16}$$

subject to the (discrete) algebraic relations

$$\rho^h = \frac{p^h_{\text{the}}}{RT^h}, \quad \mu^h = \left(\frac{T^h}{T_{\text{ref}}}\right)^{\frac{3}{2}}\left(\frac{T_{\text{ref}}+S}{T^h+S}\right)\mu_{\text{ref}}, \quad \lambda^h = \frac{c_p}{\text{Pr}}\mu^h. \tag{17}$$

The thermodynamic pressure p^h_{the} may be a function of T^h via

$$p^h_{\text{the}} = \frac{RM_0}{\int_\Omega \frac{1}{T^h}\,d\Omega}. \tag{18}$$

A Pressure-Stabilizing Petrov–Galerkin (PSPG) term appears in (14), and a grad-div term in (15) (last terms on the left-hand side of (14) and in the first line of (15), respectively). These two subgrid-scale terms will be kept also for the AVM^3 described below, since they are not related to a convective term as all other subgrid-scale terms described in the following. The terms in the second line of (15) are, in this order, a Streamline Upwind Petrov–Galerkin (SUPG, see, e.g., [42]), a cross-stress and a Reynolds-stress term, all of them being in convective form. Analogously, the terms in the second line of (16) may be referred to. All these subgrid-scale terms related to convective terms will be replaced in the context of the AVM^3.

As in [28], the stabilization parameters τ_{M} and τ_{C} proposed for incompressible flow in [29] are adopted for the present variable-density equation system:

$$\tau_{\text{M}} = \frac{1}{\sqrt{\left(\frac{2\rho^h}{\Delta t}\right)^2 + (\rho\mathbf{u})^h\cdot\mathbf{G}(\rho\mathbf{u})^h + C_{\text{I}}(\mu^h)^2\mathbf{G}:\mathbf{G}}}, \tag{19}$$

$$\tau_{\text{C}} = \frac{1}{\tau_{\text{M}}\mathbf{g}\cdot\mathbf{g}},$$

where

$$G_{ij} = \sum_{k=1}^{3}\frac{\partial\xi_k}{\partial x_i}\frac{\partial\xi_k}{\partial x_j}, \quad g_i = \sum_{j=1}^{3}\frac{\partial\xi_j}{\partial x_i},$$

utilize the coordinate system ξ of the element parent domain; see, e.g., [43] for elaboration. The time-step length of the temporal discretization of the problem formulation is denoted by Δt, and C_{I} is a positive constant independent of the characteristic element length h. Adopting (19) for the energy-conservation equation yields

$$\tau_{\text{E}} = \frac{1}{\sqrt{\left(\frac{2\rho^h}{\Delta t}\right)^2 + (\rho\mathbf{u})^h\cdot\mathbf{G}(\rho\mathbf{u})^h + C_{\text{I}}\left(\frac{\lambda^h}{c_p}\right)^2\mathbf{G}:\mathbf{G}}}.$$

4. Generalized-α time integration and solution procedure

In principle, any time-integration scheme may be used in the present context. However, our preference is on the generalized-α scheme, which was originally proposed for the compressible formulation of the Navier–Stokes equations in [44], in a form we already used for incompressible flow problems in [45]. In this section, the application is demonstrated for the (simpler) case of the energy-conservation equation, for reasons of brevity. The matrix formulation of (16) using the generalized-α scheme is given as

$$\mathbf{M}\dot{\mathbf{T}}^{n+\alpha_{\text{m}}} + \left(\mathbf{C}^{n+\alpha_{\text{f}}} + \mathbf{C}^{n+\alpha_{\text{f}}}_{\text{VM}} + \mathbf{D}\right)\mathbf{T}^{n+\alpha_{\text{f}}} = \mathbf{f}^{n+\alpha_{\text{f}}}_{\text{E}},$$

where $\mathbf{M}, \mathbf{C}^{n+\alpha_{\text{f}}} = \mathbf{C}(\mathbf{U}^{n+\alpha_{\text{f}}}), \mathbf{C}^{n+\alpha_{\text{f}}}_{\text{VM}} = \mathbf{C}_{\text{VM}}(\mathbf{U}^{n+\alpha_{\text{f}}})$ and $\mathbf{D}$ denote the matrices containing the transient, the (non-linear) convective standard Galerkin and variational multiscale (i.e., SUPG, cross- and Reynolds-stress), and viscous term on the left-hand side. The right-hand-side terms are evaluated at $n+\alpha_{\text{f}}$ and constitute the vector $\mathbf{f}^{n+\alpha_{\text{f}}}_{\text{E}}$. As indicated, the convective term of the energy-conservation equation depends on the velocity solution at $n+\alpha_{\text{f}}$, which is obtained as a result of the momentum–conservation equation. The vectors $\dot{\mathbf{T}}^{n+\alpha_{\text{m}}}$ and $\mathbf{T}^{n+\alpha_{\text{f}}}$ contain the degrees of freedom for the temporal derivative and the actual value of the temperature at the respective points in time subject to

$$\mathbf{T}^{n+1} = \mathbf{T}^n + \gamma\Delta t\dot{\mathbf{T}}^{n+1} + (1-\gamma)\Delta t\dot{\mathbf{T}}^n,$$

$$\dot{\mathbf{T}}^{n+\alpha_{\text{m}}} = \alpha_{\text{m}}\dot{\mathbf{T}}^{n+1} + (1-\alpha_{\text{m}})\dot{\mathbf{T}}^n,$$

$$\mathbf{T}^{n+\alpha_{\text{f}}} = \alpha_{\text{f}}\mathbf{T}^{n+1} + (1-\alpha_{\text{f}})\mathbf{T}^n.$$

According to [44], second-order accuracy is achieved if

$$\gamma = \frac{1}{2} + \alpha_{\text{m}} - \alpha_{\text{f}} \tag{20}$$

and unconditional stability if $\alpha_m \geqslant \alpha_f \geqslant \frac{1}{2}$. Choosing one parameter, ρ_∞, which controls the amount of high-frequency dissipation, all other parameters are defined via

$$\alpha_m = \frac{1}{2}\left(\frac{3-\rho_\infty}{1+\rho_\infty}\right), \quad \alpha_f = \frac{1}{1+\rho_\infty}$$

and (20). Our choice in this study, which is the one also suggested in [44] and used in our previous studies, is $\rho_\infty = 1/2$, resulting in $\alpha_m = 5/6$, $\alpha_f = 2/3$ and $\gamma = 2/3$.

The coupled system of energy-conservation equation, on the one hand, and mass-/momentum–conservation equation, on the other hand, is solved iteratively. At the beginning of each time step, it is first solved for the energy-conservation equation and then for the mass-/momentum–conservation equation, with a potentially required solution of the equation for the thermodynamic pressure (18) in between. Algebraic Eq. (17) are evaluated at the Gaussian integration points when necessary. Depending on the prescribed number of iterations or on whether a prescribed tolerance criterion has not yet been achieved, further (outer) iterations may be performed; further (inner) iterations of the sub-problems are not performed. At the end of each time step, it is finally solved for the energy-conservation equation another time, as this procedure already turned out instrumental in better maintaining conservation in [14]. It is accounted for the non-linearity of the coupled system by using a Picard (or fixed-point-like) iteration scheme based on an incremental formulation of both matrix systems.

Hence, in terms of the energy-conservation equation, it is iteratively solved for increments $\Delta\mathbf{T}^{n+1,i+1} = \mathbf{T}^{n+1,i+1} - \mathbf{T}^{n+1,i}$ in each iteration step $i+1$, where $i \geqslant 0$. To start the iteration in each time step, the same-velocity predictor proposed in [44] is adopted for mass and momentum conservation. The analogue, that is, a same-temperature predictor is used for the energy-conservation equation: $\mathbf{T}^{n+1,0} = \mathbf{T}^n$ and $\dot{\mathbf{T}}^{n+1,0} = ((\gamma-1)/\gamma)\dot{\mathbf{T}}^n$. The iteration for the increments operates on the residual vector $\mathbf{R}_E^i = \mathbf{M}\dot{\mathbf{T}}^{n+\alpha_m,i} + (\mathbf{C}^{n+\alpha_f,i} + \mathbf{D})\mathbf{T}^{n+\alpha_f,i} - \mathbf{f}_E^{n+\alpha_f,i}$. To obtain the respective matrices as approximations of the consistent tangent matrices, partial derivatives as

$$\frac{\partial \dot{\mathbf{T}}^{n+\alpha_m}}{\partial \mathbf{T}^{n+1}} = \frac{\partial \dot{\mathbf{T}}^{n+\alpha_m}}{\partial \dot{\mathbf{T}}^{n+1}}\frac{\partial \dot{\mathbf{T}}^{n+1}}{\partial \mathbf{T}^{n+1}} = \frac{\alpha_m}{\gamma\Delta t},$$
$$\frac{\partial \mathbf{T}^{n+\alpha_f}}{\partial \mathbf{T}^{n+1}} = \alpha_f,$$

are taken, yielding the formulation for the increments $\Delta\mathbf{T}^{n+1,i+1}$:

$$\left[\mathbf{M} + \alpha_f\frac{\gamma\Delta t}{\alpha_m}\left(\mathbf{C}^{n+\alpha_f,i} + \mathbf{C}_{VM}^{n+\alpha_f,i} + \mathbf{D}\right)\right]\Delta\mathbf{T}^{n+1,i+1} = -\frac{\gamma\Delta t}{\alpha_m}\mathbf{R}_E^i.$$

5. Algebraic variational multiscale–multigrid method

For introducing small-scale subgrid-viscosity and subgrid-diffusivity terms, the resolved part of the velocity and the temperature is further decomposed into a large resolved and a small resolved part, while keeping the unresolved part as in (12):

$$\mathbf{u} = \underbrace{\mathbf{u}^{3h} + \delta\mathbf{u}^h}_{\mathbf{u}^h} + \hat{\mathbf{u}}, \quad T = \underbrace{T^{3h} + \delta T^h}_{T^h} + \widehat{T}.$$

The space of large resolved velocity scales is identified by a grid of characteristic element length $3h$, whereas the full resolution limit is h. The actual implementation proposed in the present study performs this separation in a purely algebraic way without need for generating additional grid levels besides the basic one, though. The procedure of further decomposing the equation governing the resolved scales into equations governing large and small resolved scales, respectively, is not described here. The reader is referred to our earlier publications such as [40,3,32,45] for elaboration.

5.1. Small-scale subgrid viscosity and diffusivity

The small-scale subgrid-viscosity term is based on the physical reasoning that energy transport in turbulent flow mainly occurs between scales of similar size. The present model should particularly account for the effect of unresolved scales on the small resolved scales. The subgrid viscosity, $\mu_T^{\delta h}$, is assumed to only depend on the small resolved scales. It is defined by a modified (constant-coefficient) Smagorinsky model [46] as

$$\mu_T^{\delta h} = \rho^h (C_S h)^2 \left|\varepsilon(\delta\mathbf{u}^h)\right|,$$

with C_S denoting the Smagorinsky constant and $|\varepsilon(\delta\mathbf{u}^h)| = \sqrt{2\varepsilon(\delta\mathbf{u}^h) : \varepsilon(\delta\mathbf{u}^h)}$ the norm of the rate-of-deformation tensor based on the small-scale velocity. As for the turbulent incompressible flow examples in [32,45], the Smagorinsky constant C_S is chosen to be 0.1, that is, Deardorff's [47] original proposal for turbulent (incompressible) channel flow. No parameter tuning is performed to keep the modeling as simple as possible. A small-scale subgrid-diffusivity term in analogy to the respective "all-scale" term used, e.g., in [17] is given as

$$\left(\frac{\lambda}{c_p}\right)_{\mathrm{T}}^{\delta h} = \frac{\mu_{\mathrm{T}}^{\delta h}}{\mathrm{Pr}_{\mathrm{T}}},$$

where Pr_{T} denotes the turbulent Prandtl number, for which a constant value $\mathrm{Pr}_{\mathrm{T}} = 0.9$ will be assumed for all numerical test cases below. This value is based on numerical evidence in [48,14] for turbulent variable-density flow in a channel configuration. However, the same value will also be used for the Rayleigh–Taylor instability and turbulent flow over a backward-facing step with heating, following the same rationale as for the Smagorinsky constant above, that is, the avoidance of any parameter tuning.

With the aid of the small-scale modeling terms, the terms accounting for the unresolved scales in the convective part in Eqs. (15) and (16) may be replaced to obtain

$$\begin{aligned}&\left(\mathbf{v}^h, \rho^h \frac{\partial \mathbf{u}^h}{\partial t}\right) + \left(\mathbf{v}^h, \rho^h \mathbf{u}^h \cdot \nabla \mathbf{u}^h\right) + \left(\nabla \cdot \mathbf{v}^h, p_{\mathrm{hyd}}^h\right) + \left(\varepsilon(\mathbf{v}^h), 2\mu^h \varepsilon'(\mathbf{u}^h)\right) + \left(\nabla \cdot \mathbf{v}^h, \tau_{\mathrm{C}} \mathcal{R}^h{}_{\mathrm{C}}\right) + \left(\varepsilon(\delta \mathbf{v}^h), 2\mu_{\mathrm{T}}^{\delta h} \varepsilon'(\delta \mathbf{u}^h)\right) \\ &= \left(\mathbf{v}^h, \rho^h \mathbf{g}\right) + \left(\mathbf{v}^h, \mathbf{h}_{\mathbf{u}}\right)_{\Gamma_{\mathrm{N,u}}} \quad \forall \mathbf{v}^h \in \mathcal{V}_{\mathbf{u}}^h, \end{aligned} \tag{21}$$

$$\begin{aligned}&\left(w^h, \rho^h \frac{\partial T^h}{\partial t}\right) + \left(w^h, \rho^h \mathbf{u}^h \cdot \nabla T^h\right) + \left(\nabla w^h, \frac{\lambda^h}{c_p} \nabla T^h\right) + \left(\nabla \delta w^h, \left(\frac{\lambda}{c_p}\right)_{\mathrm{T}}^{\delta h} \nabla \delta T^h\right) \\ &= \left(w^h, \frac{1}{c_p}\left[\frac{dp_{\mathrm{the}}^h}{dt} + Q\right]\right) + \left(w^h, h_{\mathrm{T}}\right)_{\Gamma_{\mathrm{N,T}}} \quad \forall w^h \in \mathcal{V}_T^h. \end{aligned} \tag{22}$$

The small-scale modeling terms are represented by the first term in the second line of both equations. It is noted that an artificial small-scale subgrid-diffusivity term of different type (i.e., with an artificial kinematic subgrid diffusivity $\kappa^{\mathrm{art}} = Ch$, where C is a (bounded) parameter with dimension of a velocity) was proposed in [49] for *stabilizing* FE formulations.

5.2. Scale separation by plain aggregation algebraic multigrid

Plain aggregation algebraic multigrid (PA-AMG) is used for generating prolongation and restriction (i.e., level-transfer) operator matrices based on algebraic principles. According to this, a prolongation operator matrix $\mathbf{P}_{3h}^h$ is generated, see [31,32] for elaboration. Originally, PA-AMG was developed in the framework of smoothed aggregation multigrid (SA-AMG) solvers, which were introduced in [50]. The restriction operator matrix $\mathbf{R}_h^{3h}$ is chosen to be the transpose of the prolongation operator matrix:

$$\mathbf{R}_h^{3h} = \left(\mathbf{P}_{3h}^h\right)^{\mathrm{T}}$$

and it holds that $\mathbf{R}_h^{3h}\ \mathbf{P}_{3h}^h = \mathbf{I}$. A scale-separating operator matrix is defined as $\mathbf{S}_h^{3h} = \mathbf{P}_{3h}^h \mathbf{R}_h^{3h}$, in analogy to the scale-separating operator in [40].

The matrix containing the small-scale subgrid-diffusivity term, $\mathbf{D}_{\mathrm{ss}}$, is added to the incremental matrix system as follows:

$$\left[\mathbf{M} + \alpha_{\mathrm{f}} \frac{\gamma \Delta t}{\alpha_{\mathrm{m}}}\left(\mathbf{C}^{n+\alpha_{\mathrm{f}},i} + \mathbf{D} + \beta \mathbf{D}_{\mathrm{ss}}\left[\mathbf{I} - \mathbf{S}_h^{3h}\right]\right)\right] \Delta \mathbf{T}_{n+1,i+1} = -\frac{\gamma \Delta t}{\alpha_{\mathrm{m}}}\left(\mathbf{R}_{\mathrm{E}}^i + \mathbf{D}_{\mathrm{ss}}\left[\mathbf{I} - \mathbf{S}_h^{3h}\right]\mathbf{T}^{n+\alpha_{\mathrm{f}},i}\right), \tag{23}$$

where the parameter β may be chosen to be either zero or one. Note that matrix $\mathbf{D}_{\mathrm{ss}}$ is only added to the small resolved scales via the scale-separating operator matrix $\mathbf{S}_h^{3h}$. A similar procedure is applied to the matrix system resulting from mass and momentum conservation using the matrix containing the small-scale subgrid-viscosity term. The reader is referred to [32,45] for elaboration and the depiction of the final matrix system in the context of incompressible flow, which only marginally changes in the present context.

Parameter β allows for applying a Picard (or fixed-point-like) iteration scheme to the small-scale modeling term ($\beta = 1$), as used for all other terms, but also for employing a computationally much more efficient fixed-point iteration scheme ($\beta = 0$). For $\beta = 0$, only a small-scale temperature vector $\delta \mathbf{T}^{n+\alpha_{\mathrm{f}},i} = [\mathbf{I} - \mathbf{S}_h^{3h}]\mathbf{T}^{n+\alpha_{\mathrm{f}},i}$ needs to be calculated and may then be used within the usual assembly process of the right-hand side of (23) without notable additional computing effort. Furthermore, a more densely populated matrix due to the addition of $\mathbf{D}_{\mathrm{ss}}[\mathbf{I} - \mathbf{S}_h^{3h}]$ to the left-hand side with respect to all other matrices is circumvented; such a higher population density usually poses an additional challenge for the solver. Due to these reasons, $\beta = 0$ is chosen in the numerical examples below.

Remark 5.1. The particular way of implementing the scale separation, $\mathbf{D}_{\mathrm{ss}}[\mathbf{I} - \mathbf{S}_h^{3h}]$, is a so-called "one-sided" scale separation, in contrast to the "two-sided" version $[\mathbf{I} - \mathbf{S}_h^{3h}]^{\mathrm{T}}\mathbf{D}_{\mathrm{ss}}[\mathbf{I} - \mathbf{S}_h^{3h}]$. As shown in [32], the one-sided version is computationally more efficient. In case of a projective scale separation, as provided by using PA-AMG scale-separating operators, one- and two-sided scale separation are expected to be equivalent. This was confirmed by means of a Fourier analysis in [45].

6. Numerical examples

The first numerical example, a Rayleigh–Taylor instability, is investigated for a mixture-fraction formulation as given in (6)–(8). The more elaborately presented temperature-based formulation is used for the other two numerical examples, that is, turbulent flow in a channel with heated and cooled wall and turbulent flow over a backward-facing step with heating. All discretizations used in the following numerical examples employ (bi-/tri-) linearly interpolated elements. For solving the linear systems of equations arising at the end of the respective discretization processes, an AMG-preconditioned GMRES solver is applied.

6.1. Overview on investigated methodical combinations and results

There are basically three alternatives for accounting for the effect of the subgrid scales related to the convective terms in momentum- and energy-conservation equations:

- only the SUPG term (first term in the second line of (15) and (16), abbreviation: "SUP"),
- SUPG, cross- and Reynolds-stress terms (all terms in the second line of (15) and (16), abbreviation: "SCR"), or
- the small-scale subgrid-viscosity and -diffusivity term, respectively, via AVM^3 (first term in the second line of (21) and (22), abbreviation: "AVM").

The following six methodical combinations, where the first (three-letter) part of the six-letter abbreviation is related to the method applied to momentum and the second part to energy conservation, represent reasonable ones and were investigated for the numerical examples:

- SUPSUP, SCRSUP, SCRSCR, AVMAVM, AVMSUP, AVMSCR.

Furthermore, it was also considered adding all terms (abbreviation: "ALL") either only for momentum or both for momentum and energy conservation:

- ALLSUP, ALLSCR, ALLALL.

Finally, the combination of small-scale subgrid-viscosity and SUPG term (abbreviation: "AVS") for the momentum equation was taken into account:

- AVSSUP,

resulting in an overall number of 10 methodical combinations. PSPG and grad-div term, which are not related to the convective term, are always included.

In order to keep the number of presented results within reasonable bounds in the following, some important general results with respect to stability and robustness of the methodical combinations are already reported here in summary. All methodical combinations were sequentially tested for the three numerical examples according to the order given below, which elevates the challenges the methods are subjected to example by example. First of all, it is stated that none of the methodical combinations used for the momentum–conservation equation exhibited any indications for potential instabilities or lack of robustness. Second, however, the use of the small-scale subgrid-diffusivity term for the energy-conservation equation was identified to provoke instabilities already for turbulent channel flow with heated and cooled wall and later also for turbulent flow over a backward-facing step with heating. Finally, the addition of cross- and Reynolds-stress terms for the energy-conservation equation caused instabilities for turbulent flow over a backward-facing step with heating. Closer investigations specified their initial occurence within the lower-wall region where substantial temperature variations prevail, as will be shown below. Furthermore, it appeared that rather the Reynolds-stress term, which incorporates both the residual of the momentum- and of the energy-conservation equation (see last term in second line of (16)), than the cross-stress term was responsible for the instabilities.

As a result, it is focused on an SUPG method for the numerical approximation of the energy-conservation equation, which turned out to be the most robust approach for this, and thus, four of the aforementioned methodical combinations: three versions of the proposed AVM^3, that is, AVMSUP, AVSSUP, and ALLSUP, are preferably compared to the residual-based method SCRSUP, which takes also into account cross- and Reynolds-stress terms for the momentum–conservation equation as proposed in [29]. The addition of cross- and Reynolds-stress terms and/or a small-scale subgrid-diffusivity term for the energy-conservation equation did not provide notably superior results in all stable simulations either.

6.2. Rayleigh–Taylor instability

In the first numerical example, the basic ability of the respective methodical combinations to accurately simulate variable-density flows with high density ratios is investigated for the case of a two-dimensional Rayleigh–Taylor instability

problem. The set-up is analogous to the one in [16]. The problem domain is $\Omega = [-L_1, L_1] \times [-L_2, L_2]$ with $L_1 = L_2 = 0.5$. Two miscible fluids, that is, a heavy fluid with density $\rho_H = 1.0$ above a light fluid with density $\rho_L = 0.1$, are initially separated by an interface located at

$$x_2^{\text{int}}(x_1) = -\alpha \sum_{k=1}^{7} \cos(\omega_k \pi x)$$

with wave amplitude $\alpha = 0.001$ and wave numbers $\omega_k = 4$, 14, 23, 28, 33, 42, 51 and 59 as proposed in [51]. Furthermore, initial values are a zero velocity field and a mixture-fraction distribution as

$$Z(x_2, x_1) = \frac{1}{2}\left(1 + \tanh\left(\frac{x_2^{\text{int}}(x_1) - x_2}{2\delta}\right)\right),$$

where the thickness of the interface is $\delta = 0.002$.

Periodic boundary conditions are assumed at the vertical boundaries. No-slip boundary conditions and mixture fractions $Z = 1$ and $Z = 0$ are prescribed at the lower and upper horizontal boundary, respectively. Both fluids are assumed to have the same kinematic viscosity $\nu = \mu/\rho = 0.001$ and the same kinematic diffusivity $D_Z = 0.0005$. A gravity acceleration $g = 9.0$ is prescribed, resulting in a Reynolds number $\text{Re} = \sqrt{gL_2}L_1/\nu = 3000$. Four different spatial discretizations with $n_{\text{el}} = 64$, 128, 256 and 512 finite elements in both spatial directions are employed. As in [16], the solution using 512×512 elements is assumed to provide a reference solution for the solutions obtained on the coarser discretizations. A constant time-step length $\Delta t = 0.001$ is applied to all spatial resolutions. The simulations are advanced until $t_{\text{end}} = 0.75$ to obtain the following data. An impression of the solution is provided in Fig. 1, exemplarily depicting the velocity distribution along with velocity vectors as well as the mixture-fraction distribution along with contours obtained via AVMSUP on the finest discretization.

Fig. 2 depicts the mixture-fraction contours obtained for various discretizations using AVMSUP. Density profiles at $x_2 = 0.20$ for various discretizations and methods are evaluated in Fig. 3. The contour plots reveal that a discretization using 64×64 elements is not sufficient for resolving the mixture-fraction distribution; hence, it is not included in the density profiles depicted in Fig. 3 (left graph). Using 128×128 elements, both contours and density profile approach the reference contours and profile obtained with 512×512 elements. However, there are still differences, particularly observable for the density profiles in form of reversed peak locations. Notable convergence to the reference contours and profile is observed for 256×256 elements. As also shown, the present profile obtained for 512×512 elements is very close to the one obtained in [16] for a sixth-order finite difference formulation on a 128×128 grid. The convergence of the mean values of mixture fraction in Ω is quantified in Table 1.

As the right graph in Fig. 3 indicates, there is not any notable difference between the various methods considered on a 256×256 discretization. A quantification via mean values of mixture fraction is provided in Table 2. AVMSUP predicts a mean value marginally closer to the reference value on a discretization with 512×512 than the other methods. Such very limited differences are to be expected, since there are no "real" turbulence effects in this example. Thus, we do not expect substantial benefits from including the small-scale subgrid-viscosity term. Vice versa, however, it is demonstrated that the inclusion of this small-scale term does not degrade the results for such a non-turbulent problem configuration with high density ratio. This is in contrast to standard subgrid-viscosity models such as the (all-scale) Smagorinsky model, which are known to be often over-dissipative in laminar and transitional situations.

6.3. Turbulent channel flow with heated and cooled wall

Turbulent channel flow at Reynolds number $\text{Re}_\tau = \frac{\rho u_\tau \delta_c}{\mu} = 180$ and (molecular) Prandtl number $\text{Pr} = 0.71$ with a heated wall at temperature T_H and a cooled wall at temperature T_C is studied. This Reynolds number appears to represent the case

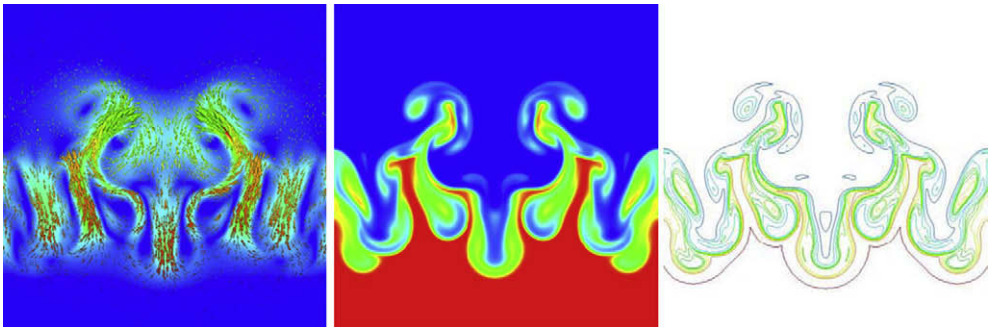

Fig. 1. Rayleigh–Taylor instability problem at $t_{\text{end}} = 0.75$ using AVMSUP on 512×512 elements, left: velocity vectors on colored velocity magnitude distribution, middle: colored mixture-fraction distribution, right: colored mixture-fraction contours (red color indicates high velocity/mixture fraction, blue color low velocity/mixture fraction). (For interpretation of the references to colour in this figure legend, the reader is referred to the web version of this article.)

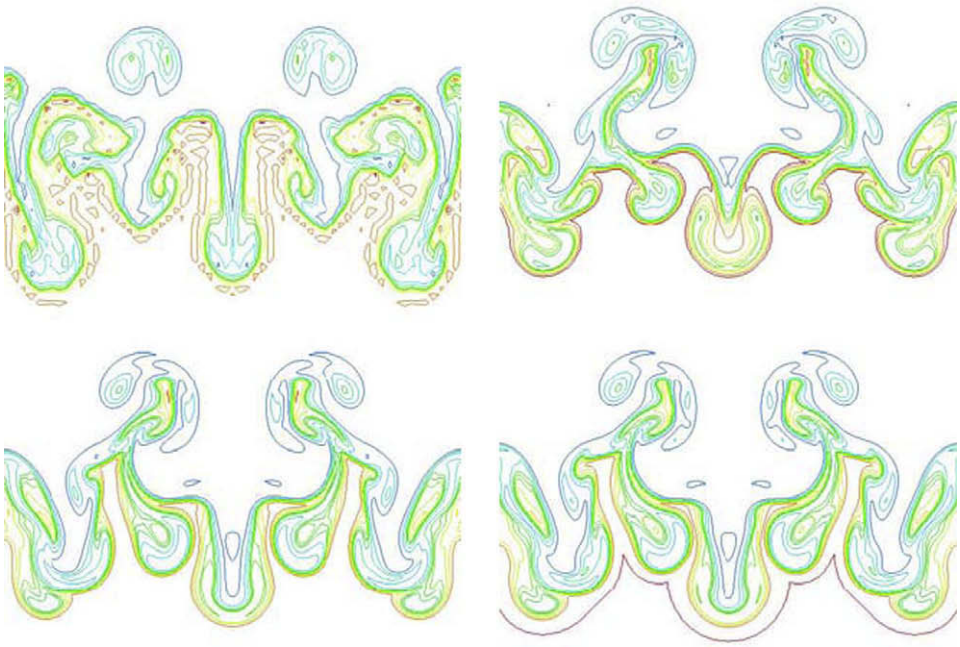

Fig. 2. Mixture-fraction contours for Rayleigh–Taylor instability problem at $t_{end} = 0.75$ on various discretizations using AVMSUP, from left to right and top to bottom: 64×64, 128×128, 256×256, 512×512 elements.

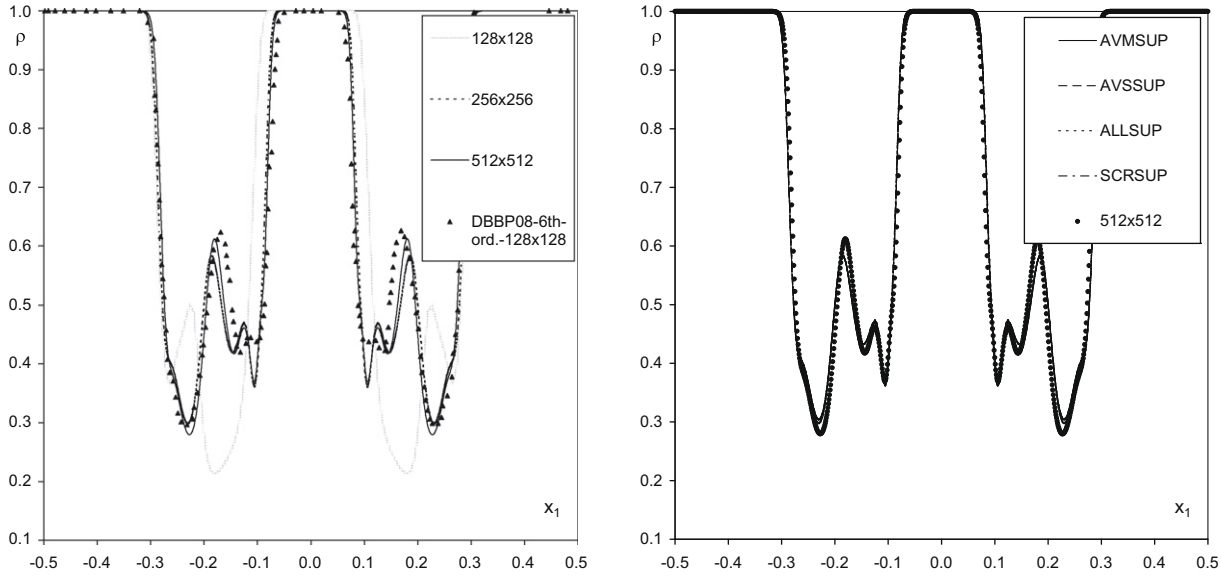

Fig. 3. Density profiles at $x_2 = 0.20$ for Rayleigh–Taylor instability problem at $t_{end} = 0.75$, left: AVMSUP on various discretizations, right: various methods on discretization with 256×256 elements.

Table 1
Mean values of mixture fraction in Ω for Rayleigh–Taylor instability problem at $t_{end} = 0.75$ on various discretizations using AVMSUP.

	$\overline{Z}$
64×64	0.3978
128×128	0.3721
256×256	0.3651
512×512	0.3637

Table 2
Mean values of mixture fraction in Ω for Rayleigh–Taylor instability problem at $t_{end} = 0.75$ using 256×256 elements and various methods.

	$\overline{Z}$
AVMSUP	0.3651
AVSSUP	0.3652
ALLSUP	0.3653
SCRSUP	0.3653

almost exclusively studied in the context of turbulent low-Mach-number flow. DNS data for this Reynolds number and various temperature ratios T_H/T_C are provided in [52,53], and LES were reported, e.g., in [11,14]. Here, temperature ratios $T_H/T_C = 1.01$ and $T_H/T_C = 2.00$ are investigated. For these two cases, various DNS results are given in [52,53], particularly in [52]. Those data are marked by "DNS N98" and "DNS N00", respectively, when used in the following. Furthermore, DNS data which were used in [14] for comparison and indicated therein to originate from [54] are marked by "DNS DR04". Choosing the lower temperature ratio also offers the opportunity to compare the respective velocity results to the well-established incompressible DNS data in [55], denoted by "DNS MKM99" below, since this case is very close to the incompressible (isothermal) case due to the very mild temperature ratio.

The channel dimensions are chosen to be $L_1 \times L_2 \times L_3 = 2\pi\delta_c \times \delta_c \times \frac{4}{3}\pi\delta_c$. A parabolic velocity profile in x_1-direction perturbed by random velocity fluctuations of amplitude up to 30% of the streamwise bulk mean velocity in all spatial directions represents the initial condition $\mathbf{u}_0$ for the velocity field. As usual in the aforementioned DNS and LES studies of this case, scaled initial temperature and density fields $T_0 = \rho_0 = 1.0$ are prescribed, which also represent the respective reference values, and a gas constant $R = 1.0$ is assumed. No-slip boundary conditions are applied at the upper and lower wall. Within several initial time steps, the lower wall is cooled down and the upper wall heated up such that the target temperature ratios are achieved. In the homogeneous x_1 and x_3-direction, periodic boundary conditions for velocity and temperature are applied. As driving mechanism for the flow, a body force is imposed in form of a driving pressure gradient in the streamwise x_1-direction. A scaled Sutherland law as proposed in [56] and used in [52,53] is employed, where $T_{ref} = 1.0$ and $S = 0.368$. The specific heat capacity at constant pressure is assumed to be $c_p = 1004.5$.

A constant time-step length $\Delta t = 0.004$ is applied, that is, expressed in wall units, $\Delta t^+ = \frac{\Delta t \rho u_\tau^2}{\mu} = 0.72$. 5000 time steps are performed to allow the flow to develop, and the statistics are collected during another 5000 time steps. During the statistical period, two Picard iterations within each time step are performed. Three different spatial discretizations with $n_{el} = 32$, 48 and 64 finite elements in all spatial directions are employed. The distribution of finite elements in wall-normal x_2-direction obeys a hyperbolic function refining towards the walls, that is, the location x_2^i of each grid node i, where $i = 0,\ldots,n_{el}$, in wall-normal direction is given as

$$x_2^i = \frac{\tanh\left(2.1\left(\frac{2i}{n_{el}} - 1\right)\right)}{\tanh(2.1)}.$$

This (symmetric) node distribution between lower and upper wall is maintained for both cases, and not specificially (unsymmetrically) adapted for the case with higher temperature ratio as, e.g., in [52,14]. In this context, it is noted that the DNS MKM99 data were recently verified in [57] using (tri-) linearly interpolated (and stabilized) finite elements. With 129 elements hyperbolically distributed in wall-normal direction, results already very close to the DNS MKM99 data were achieved at the present Reynolds number in that study. Hence, further refinement of the discretization with 64 elements by a factor of two in all spatial directions would probably bring the results very close to the DNS data for the lower temperature ratio, such that any notable differences between the methods would not be visible. As will be shown below, for the higher temperature ratio, the picture is different.

As usual, results are averaged in time within the statistical period and in space over the two homogeneous spatial directions. Velocity and temperature results marked by a superscript "+" in the following depictions are scaled by the velocity $u_\tau = \sqrt{\tau_W/\rho_W}$ or the temperature $T_\tau = q_W/(\rho_W c_p u_\tau)$, respectively, where τ_W, ρ_W and $q_W = \lambda \nabla T_W^h$ denote the wall-shear stress, density and heat flux at the (lower or upper) wall, respectively. The results are depicted against the wall-normal coordinate $x_2^+ = \frac{x_2 \rho_W u_\tau}{\mu_W}$ in non-dimensional wall units.

Fig. 4 depicts mean streamwise velocity and mean temperature results for $T_H/T_C = 1.01$, comparing them to respective DNS data. The temperature profiles are also presented against the Kader law, $\mathrm{Pr} \cdot x_2^+$, which is usually assumed to be valid in the vicinity of the walls. A refinement study for all three discretizations is shown, exemplarily using the residual-based method SCRSUP and the AVM^3-based method AVMSUP. For all discretizations, it is stated that almost all of the results obtained with AVMSUP are closer to the DNS data than the ones obtained with SCRSUP. Using the finest discretization, the temperature results yielded by AVMSUP excellently match the reference DNS profiles and the Kader law. Furthermore, it is particularly notable that the profiles obtained with AVMSUP on the medium discretization already achieve the accuracy of the profiles obtained with SCRSUP on the finest discretization for all cases depicted in Fig. 4.

The same may be observed for second-order velocity and temperature results such as root-mean-square values of streamwise velocity and temperature and correlations of streamwise velocity and temperature fluctuations depicted in Figs. 5 and 6, respectively. For the correlations of streamwise velocity and temperature fluctuations in the upper half of the channel, no

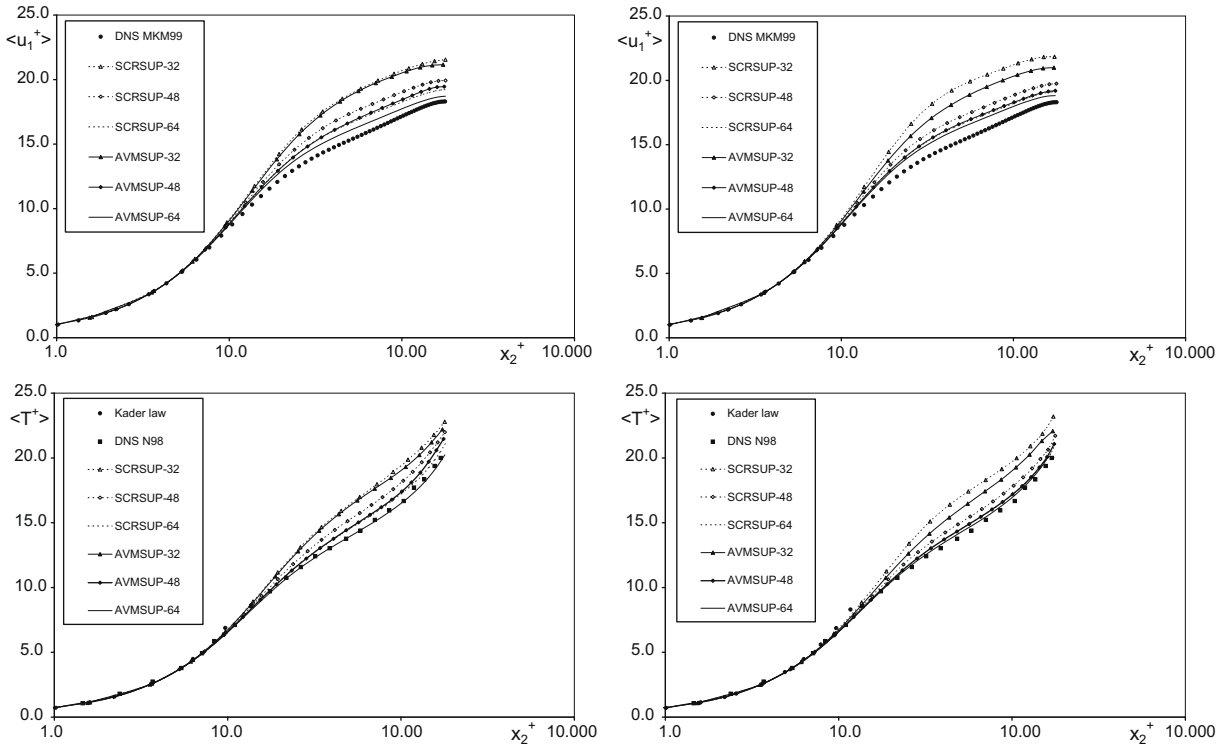

Fig. 4. Turbulent channel flow at temperature ratio $T_H/T_C = 1.01$ using AVMSUP and SCRSUP, top: mean streamwise velocity, bottom: mean temperature (left: lower channel half, right: upper channel half).

reference DNS data appear to be available in the literature; the trend observed for the lower half is mirrored to the upper half, though.

In Fig. 7, it is investigated whether beneficial effects can be expected when adding both the residual-based *and* the AVM^3-based modeling terms by comparing AVMSUP and ALLSUP for mean streamwise velocity and mean temperature results. Such a combined modeling approach was recently suggested in [58] based on a spectral analysis. As can be immediately observed, this is not the case. Further adding the residual-based modeling terms notably deteriorates the results. Cross-comparing Figs. 7 and 4 suggests that the results obtained with ALLSUP appear to be of comparable accuracy to the ones obtained with SCRSUP. Similar observations can be made for second-order velocity and temperature results such as root-mean-square values of streamwise velocity and temperature and correlations of streamwise velocity and temperature fluctuations, which are not explicitly depicted here. A similar picture is also obtained when only adding the SUPG term to the AVM^3-based modeling terms (i.e., AVSSUP), which is shown in Fig. 8.

Fig. 9 illustrates mean streamwise velocity and mean temperature results for the higher temperature ratio $T_H/T_C = 2.00$, comparing them to DNS data and the Kader law, respectively. Similar to the case with the lower temperature ratio, for all discretizations, the results predicted by AVMSUP are closer to the DNS data than the ones predicted by SCRSUP, with the only exception being the mean temperature in the lower channel half on the coarsest discretization towards the channel center. The DNS data in the upper channel half show a different behaviour towards the channel center than the converging present results. Since those data are the only reference data we are aware of in this context and the Kader law is not valid outside of the vicinity of the wall, we are not able to fully confirm these particular results.

Root-mean-square values of streamwise velocity and temperature and correlations of streamwise velocity and temperature fluctuations are shown in Figs. 10 and 11, respectively. Again for almost all profiles, the predictions by AVMSUP are closer to the reference DNS data than the ones by SCRSUP. However, it is also noted, on the one hand, that the (rather sensitive) root-mean-square temperature profiles do not follow the expected stringent convergence trend in contrast to all other values, and on the other hand, that, particularly in the lower channel half, all profiles substantially deviate from the available DNS data. A probable reason for the latter discrepancy (and also the smaller discrepancy for root-mean-square velocity profiles in the lower channel half) may be the aforementioned fact that in [52], where the DNS N98 data originate from, an unsymmetric discretization was used for $T_H/T_C = 2.00$, which was more refined towards the bottom wall. For the correlations of streamwise velocity and temperature fluctuations, no reference DNS data appear to be available in the literature; similar trends as in the case with the lower temperature ratio are clearly observable, though. The comparison of ALLSUP and AVSSUP, respectively, to AVMSUP for $T_H/T_C = 2.00$, which are depicted in Figs. 12 and 13 appears to lead to similar conclusions

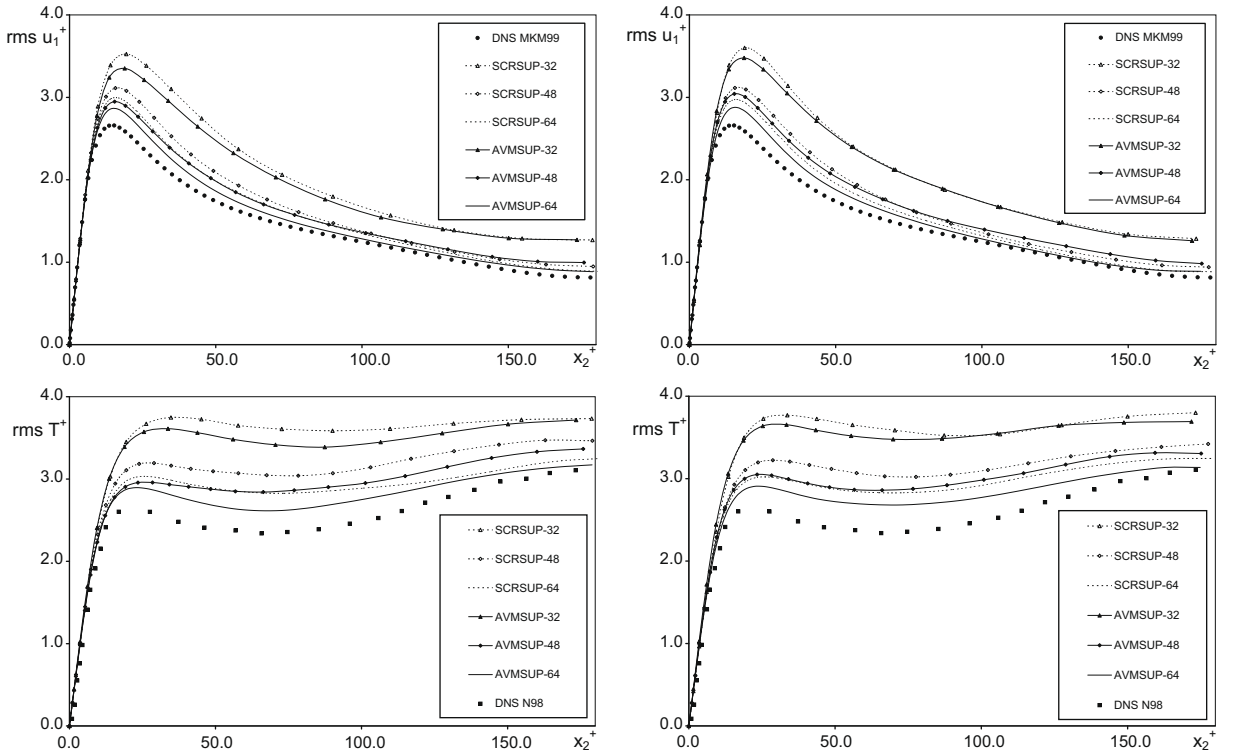

Fig. 5. Turbulent channel flow at temperature ratio $T_H/T_C = 1.01$ using AVMSUP and SCRSUP, top: root-mean-square streamwise velocity, bottom: root-mean-square temperature (left: lower channel half, right: upper channel half).

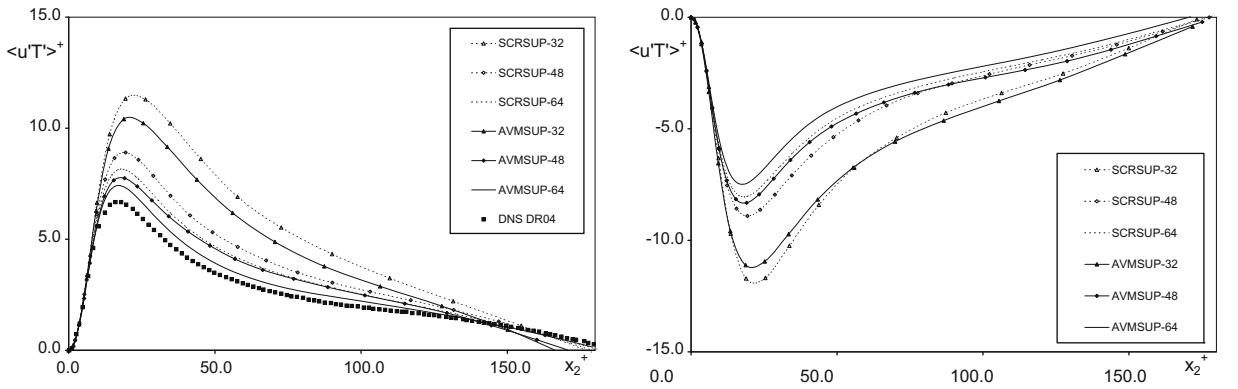

Fig. 6. Streamwise velocity-temperature fluctuations for turbulent channel flow at temperature ratio $T_H/T_C = 1.01$ using AVMSUP and SCRSUP, left: lower channel half, right: upper channel half.

with respect to potential beneficial effects when including both residual-based *and* AVM^3-based modeling terms as in the case with the lower temperature ratio, that is, such a strategy appears to be rather detrimental.

Finally, the dissipation introduced by various terms is analyzed analogously to the investigation in [59]. The dissipation due to the small-scale subgrid-viscosity term is given as

$$\epsilon_{ss} = 2\mu_T^{\delta h}\varepsilon(\delta\mathbf{u}^h)\varepsilon(\delta\mathbf{u}^h). \tag{24}$$

Measures for the dissipation due to SUPG and cross-stress terms similar to the ones in [59] in the form

$$\epsilon_{SUPG} = \rho^h\mathbf{u}^h\tau_M\mathcal{R}^h{}_M\varepsilon(\mathbf{u}^h), \tag{25}$$

$$\epsilon_{cross} = \rho^h\tau_M\mathcal{R}^h_M\mathbf{u}^h\varepsilon(\mathbf{u}^h), \tag{26}$$

respectively, are defined, which obviously yield the same value according to these definitions. When comparing the present results to the ones in [59], it must be taken into account that ϵ_{SUPG} was defined therein to contain the dissipation due to both

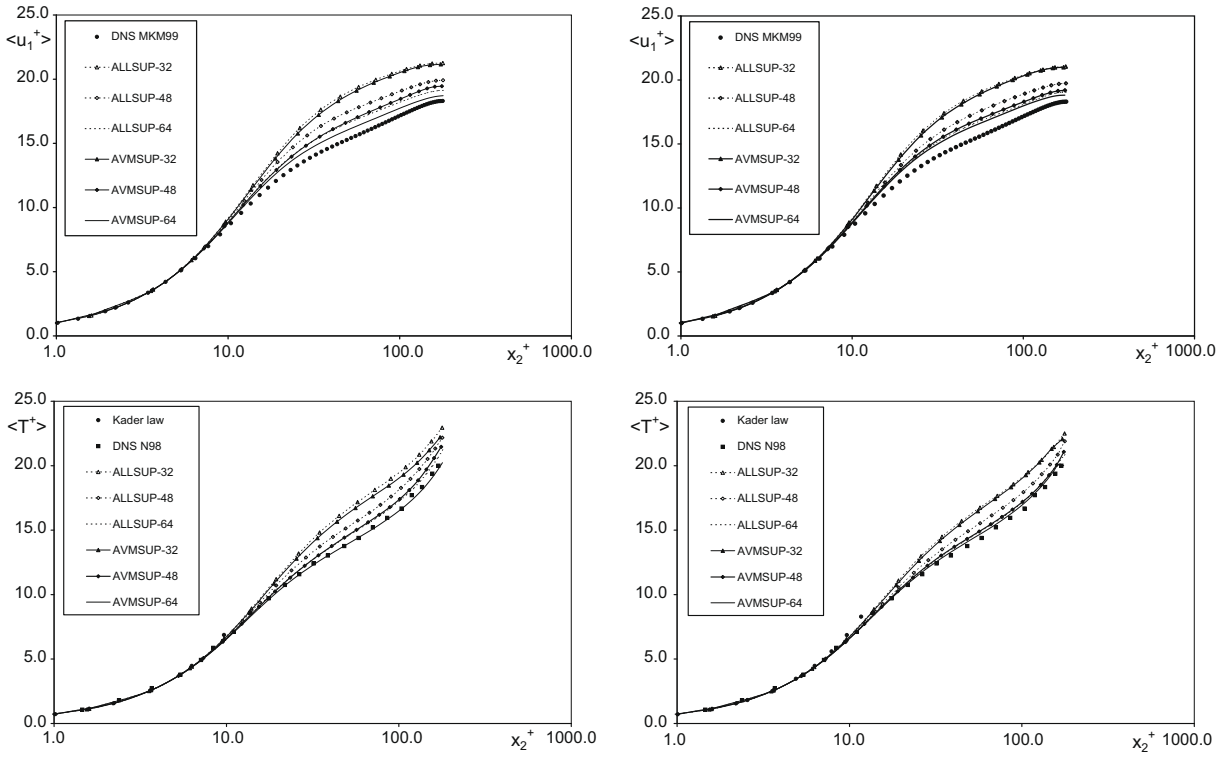

Fig. 7. Turbulent channel flow at temperature ratio $T_H/T_C = 1.01$ using AVMSUP and ALLSUP, top: mean streamwise velocity, bottom: mean temperature (left: lower channel half, right: upper channel half).

SUPG and cross-stress terms, that is, the sum of the presently defined values. Finally, an analogous measure for the dissipation due to the Reynolds-stress term is defined:

$$\epsilon_{\text{Rey}} = -\rho^h \tau_{\text{M}} \mathcal{R}^h_{\text{M}} \tau_{\text{M}} \mathcal{R}^h_{\text{M}} \mathcal{E}(\mathbf{u}^h). \tag{27}$$

For this dissipation evaluation, it is focused on the temperature ratio $T_H/T_C = 1.01$, since for this case, it is possible to compare the results to the results in [59], which were obtained for turbulent incompressible flow in a channel.

The dissipation due to the small-scale subgrid-viscosity term using ALLSUP, AVSSUP and AVMSUP on a discretization with 32 finite elements in all spatial directions is depicted in non-dimensionalized form in the left part of Fig. 14. It is observed that the introduction of dissipation is particularly pronounced close to the channel walls and almost zero in most of the inner channel region. The differences between the respective methods appear minor. In a preceding study, [40], the importance of introducing a substantial amount of subgrid viscosity to the smaller resolved scales particularly in the buffer-layer region of the channel for obtaining high-quality results was already pointed out, while the subgrid viscosity introduced in other parts of the channel appeared to be of minor relevance. The present investigation underlines that, when using the AVM^3, subgrid viscosity is indeed added to the smaller resolved scales predominantly in the vicinity of the channel walls. The distribution of dissipation due to the present small-scale subgrid viscosity in wall-normal direction is very similar to the respective distribution due to the (all-scale) dynamic-model subgrid viscosity analyzed in [59]. However, the present peak values are more than twice as large. At this point, it has to be re-emphasized that the present higher amount of subgrid viscosity is only applied to a fraction of the resolved scales, and the larger of the resolved scales remain without any (direct) addition of subgrid viscosity.

The distribution of the dissipation due to the SUPG and cross-stress term, respectively, in wall-normal direction (right part of Fig. 14) is also very similar to the respective ones depicted in [59]: this dissipation still exhibits values notably larger than zero in the inner channel region, and the peak locations are further away from the wall. For the three methods investigated, SUPSUP provides the highest and ALLSUP the lowest peak values, with SCRSUP in between, as expected. On average, the present peak values appear somewhat smaller than the ones in [59]. However, in [59], the stabilization parameter was variegated within certain bounds. As can be observed, the dissipation due to the Reynolds-stress term is much smaller compared to the dissipation due to the SUPG and cross-stress term; in fact, it turned out to be about two orders of magnitude smaller under the given circumstances. Reynolds-stress terms were not considered in [59]. Comparing the peak dissipation values due to the small-scale subgrid-viscosity term in the left part to the one due to the SUPG and cross-stress term in the right part of Fig. 14, it is stated that it is about two orders of magnitude larger than the latter.

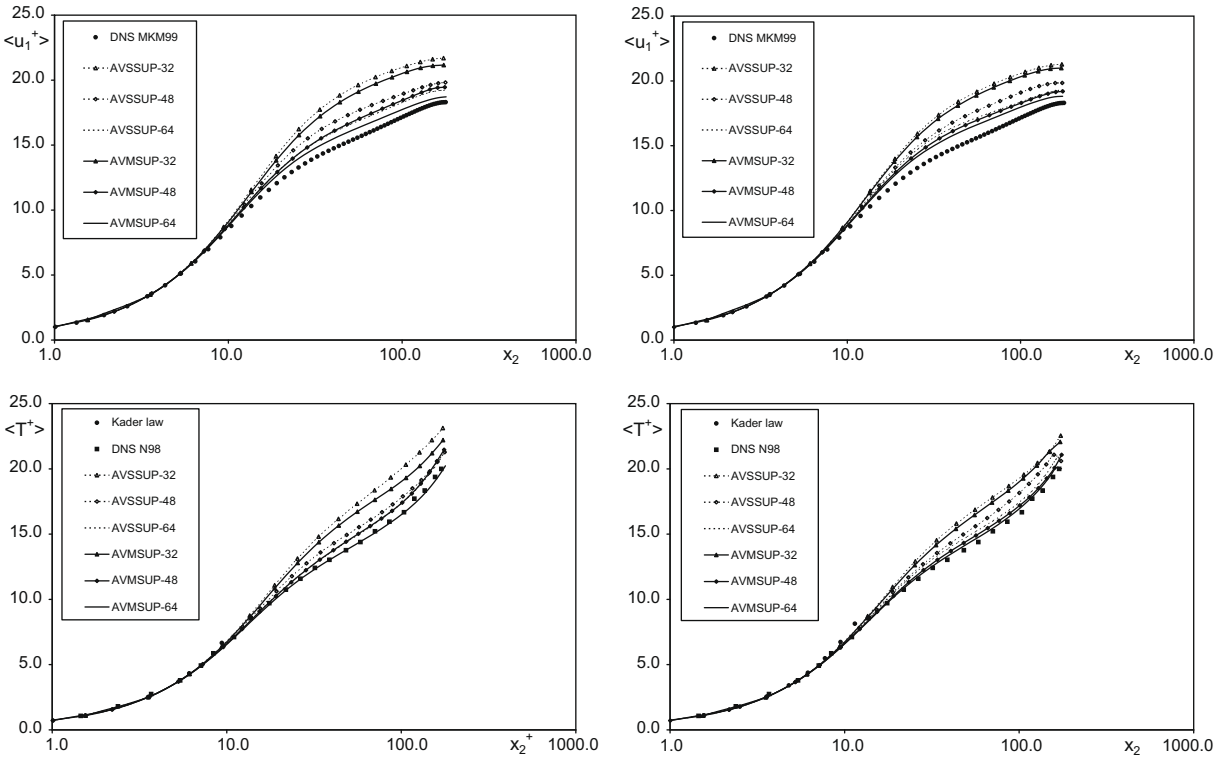

Fig. 8. Turbulent channel flow at temperature ratio $T_H/T_C = 1.01$ using AVMSUP and AVSSUP, top: mean streamwise velocity, bottom: mean temperature (left: lower channel half, right: upper channel half).

6.4. Turbulent flow over a backward-facing step with heating

As the last and most challenging numerical test case, turbulent flow over a backward-facing step with heating is considered. The Reynolds number based on the step height, which is $h = 0.041$ m, and the mean inflow centerline velocity u_{1c} is 5580. The expansion ratio, that is, the ratio of the channel height downstream and upstream of the step, is 1.5, and a wall heat flux of $q_W = 2000\ \mathrm{W/m^2}$ is prescribed at the bottom wall behind the step. The geometry of the problem domain is depicted in Fig. 15. The problem configuration is similar to the one in [13], which is the only LES of variable-density flow at low Mach number in such a configuration so far, to the best of the authors' knowledge. Given the same expansion ratio, the Reynolds number in [13] was 5540, and thus almost identical to the present one. Further wall heat fluxes besides the one used here were investigated in [13]. LES data from [13] are denoted by "LES AP02" when used below.

A comprehensive experimental study of a backward-facing step with heating was conducted in [60], though at a higher Reynolds number of 28,000 and with an expansion ratio of 1.25. LES of the present problem configuration but with substantially lower wall heat fluxes have been performed over the last couple of years in [61–63]. The low heating allows for solving the problem based on the incompressible formulation of the Navier–Stokes equations with the temperature coupled as a passive-scalar equation. Hence, variable-density effects were not taken into account in those studies. For instance, a wall heat flux of $q_W = 270\ \mathrm{W/m^2}$ was prescribed in [62,63], restricting the maximum overheat to approximately 15 K. As will be shown below, a maximum overheating of more than 400 K emerges for the present wall heat flux. Considerably more investigations of the backward-facing step without heating have been published to date. A DNS study of turbulent incompressible flow at a Reynolds number of 5100 was provided in [64]. That data, which was obtained at a Reynolds number relatively close to the present one, will also be used below, marked by "DNS LMK97". Various LES of turbulent incompressible flow within such a problem domain may also be found in the literature, an early one, for instance, in [65].

The simulations are started from an initially prescribed zero velocity field. The constant initial temperature in the problem domain is $T_0 = 293$ K, which also represents the reference temperature T_{ref}. The thermodynamic pressure, which remains constant during the simulation due to the open outflow boundary, is $p_{the} = 100{,}405\ \mathrm{J/m^3}$. With the gas constant $R = 287.0\ \mathrm{J/(kg\ K)}$ and T_0, the initial density amounts to $\rho_0 = \rho_{ref} = 1.194\ \mathrm{kg/m^3}$. The viscosity of air at the reference temperature is $\mu_{ref} = 18.23 \cdot 10^6\ \mathrm{kg/(m\ s)}$. The Prandtl number is assumed to be $Pr = 0.71$ and the specific heat capacity at constant pressure to be $c_p = 1006.0\ \mathrm{J/(kg\ K)}$. No-slip boundary conditions for the velocity are prescribed on all upper and lower (horizontal) walls as well as the (vertical) step wall. Periodic boundary conditions are assumed for both velocity and temperature in spanwise x_3-direction. At all other walls except for the bottom wall behind the step and the inflow boundary, adiabatic

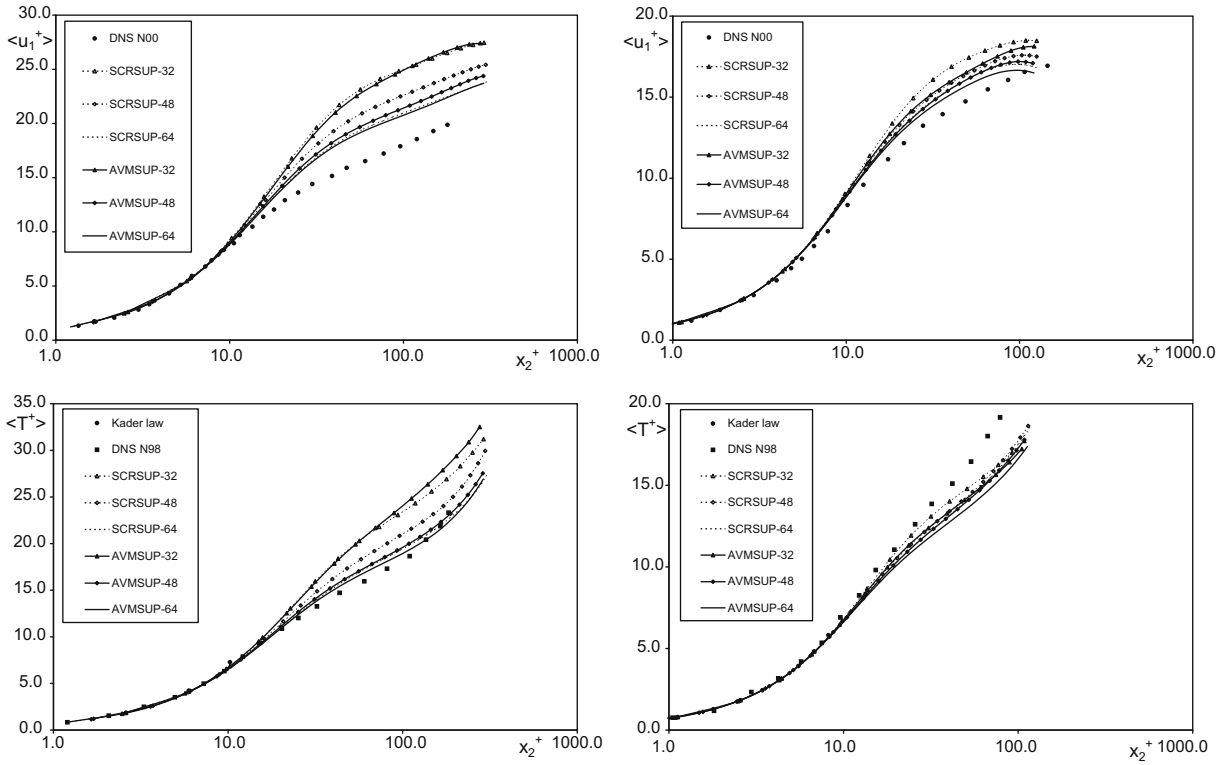

Fig. 9. Turbulent channel flow at temperature ratio $T_H/T_C = 2.00$ using AVMSUP and SCRSUP, top: mean streamwise velocity, bottom: mean temperature (left: lower channel half, right: upper channel half).

boundary conditions are prescribed for the temperature. At the inflow boundary, T_{ref} is prescribed as a Dirichlet boundary condition, and at the bottom wall behind the step, the aforementioned wall heat flux $q_W = 2000\ W/m^2$ is given.

At the outflow boundary, a zero-traction Neumann boundary condition, $\mathbf{h}_u = 0$, is assumed. As already used in [45] for turbulent incompressible flow past a square-section cylinder, a term at the outflow boundary Γ_{out} in the form $-(\mathbf{v}^h, \rho^h \mathbf{u}^h \{\mathbf{u}^h \cdot \mathbf{n}\}_-)_{\Gamma_{out}}$ has to be added to the respective FE formulation of the momentum–conservation equation, where $\{\mathbf{u}^h \cdot \mathbf{n}\}_- = \mathbf{u}^h \cdot \mathbf{n}$ if $\mathbf{u}^h \cdot \mathbf{n} < 0$ and $\{\mathbf{u}^h \cdot \mathbf{n}\}_- = 0$ otherwise; see also [41,66]. The analogous term is added here to the FE formulation of the energy-conservation equation: $-(\mathbf{v}^h, \rho^h T^h \{\mathbf{u}^h \cdot \mathbf{n}\}_-)_{\Gamma_{out}}$. The addition of these two terms ensures that potentially arising eddies at the outflow boundary are appropriately convected out of the problem domain. Usually, the most challenging condition for a flow problem such as turbulent flow over a backward-facing step amounts to be the inflow boundary condition for the velocity. Overviews on the generation of such inflow data are provided, e.g., in [67] and recently in [68]. Results from our preliminary investigations revealed that it appears sufficient for the present case to follow the simplest procedure addressed in [67,68], that is, to synthetically generate turbulent inflow data by superimposing random fluctuations on the desired mean velocity profile. The desired mean velocity profile in this context is a boundary-layer velocity profile at $Re_\tau = 285$. It is superimposed in all spatial directions by random fluctuations with a maximum amplitude of 10% of the streamwise bulk mean velocity of this boundary-layer velocity profile. The actual mean inflow centerline velocity u_{1c} is approximately 2.078 for all simulations performed, resulting in the aforementioned Reynolds number of 5580.

A constant time-step length $\Delta t = 0.008$ is applied. As for the turbulent channel flow above, 5000 time steps are performed to allow the flow to develop, and the statistics are collected during another 5000 time steps, during which two Picard iterations within each time step are performed. Non-dimensionalized by the step height and the mean inflow centerline velocity, a value $\Delta t^{\star} = \frac{\Delta t u_{1c}}{h} = 0.04$ may be calculated, which is close to $\Delta t^{\star} = 0.03$ used in [13]. As in [13], the spatial discretization is inspired by the mesh refinement studies in [69]. After all, 48 uniformly distributed elements are used in spanwise x_3-direction. In streamwise x_1-direction, 86 elements are employed overall, refined towards the step from the inflow side (18 elements) with a bias factor 1.07 and from the outflow side (68 elements) with a bias factor 1.045. In wall-normal x_2-direction, 32 elements are arranged above the step and 16 elements below, refined towards both the upper (bias factor 1.27) and the lower (bias factor 1.65) wall as well as the (virtual) horizontal step line (bias factor 1.27 from above and 1.65 from below). Hence, approximately 1 mio. degrees of freedom, that is, hydrodynamic pressure, velocity and temperature, are solved for overall.

The results presented for this example are obtained with SUPSUP, SCRSUP, AVSSUP and ALLSUP. AVSSUP is used here in preference to AVMSUP due its notably improved convergence behaviour of the AMG-preconditioned GMRES solver for the

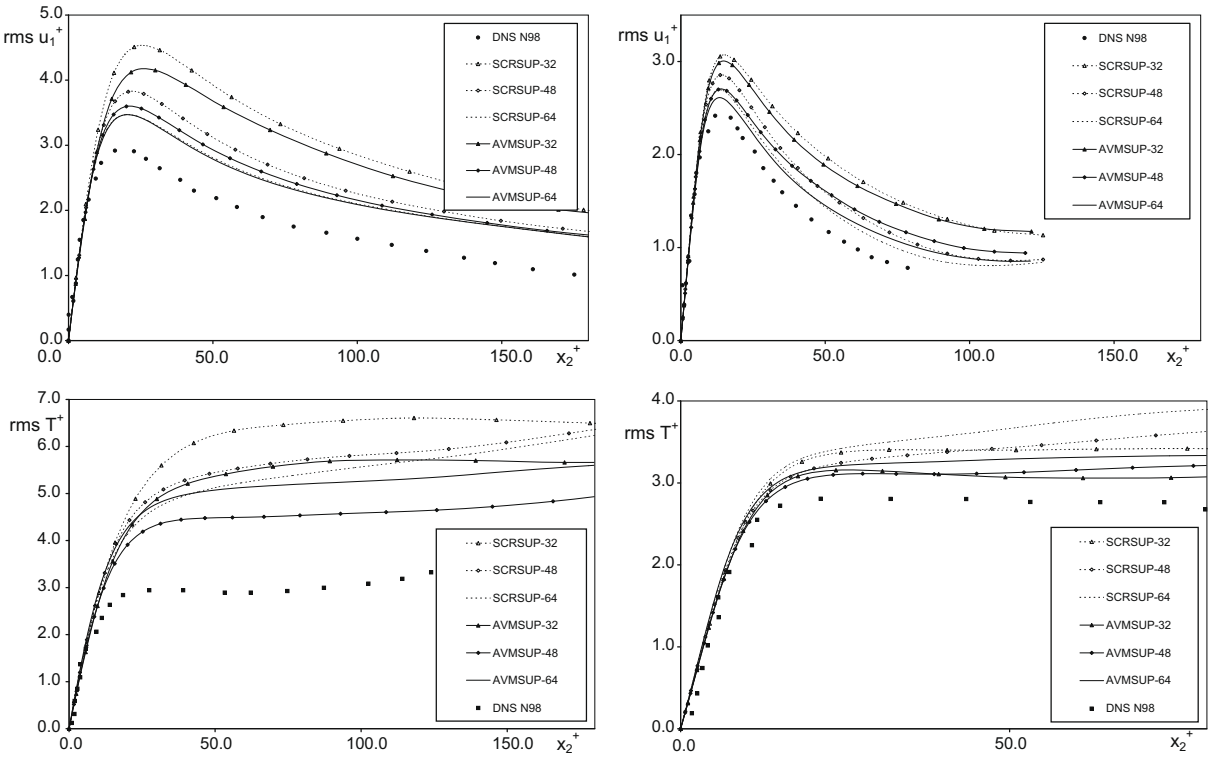

Fig. 10. Turbulent channel flow at temperature ratio $T_H/T_C = 2.00$ using AVMSUP and SCRSUP, top: root-mean-square streamwise velocity, bottom: root-mean-square temperature (left: lower channel half, right: upper channel half).

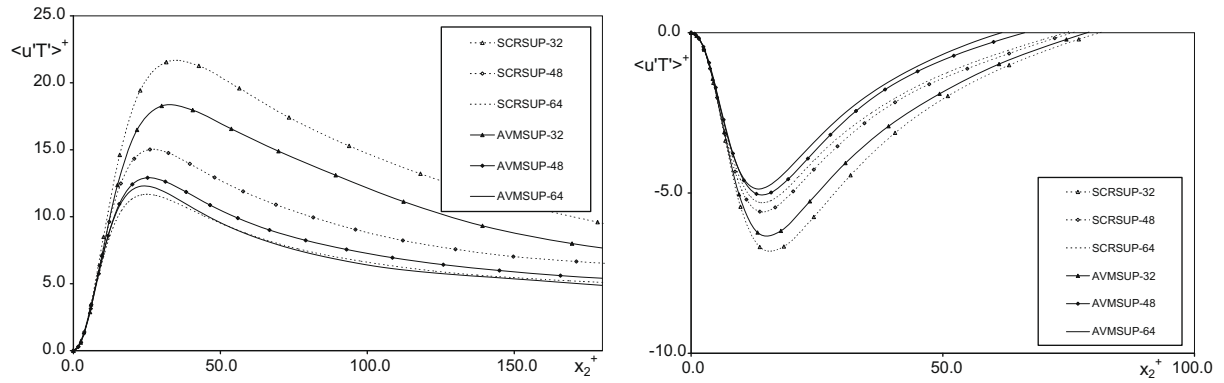

Fig. 11. Streamwise velocity-temperature fluctuations for turbulent channel flow at temperature ratio $T_H/T_C = 1.01$ using AVMSUP and SCRSUP, left: lower channel half, right: upper channel half.

present case. In fact, the inclusion of the SUPG term in the solution of the momentum equation appears to be crucial for guaranteeing an acceptable convergence of the solver. Furthermore, the SUPSUP case represents the minimum amount of modeling terms with which a stable and acceptably converging solution was enabled for the present case. Results from test simulations with less modeling terms included indeed confirmed our initial suspicion in this context.

Snapshots of velocity and temperature distributions at the beginning of the statistical period are provided in Fig. 16; the hot spots at the heated bottom wall in the vicinity of the step wall are clearly observable. Velocity results at various locations behind the step (for the lower region of the problem domain) are depicted in Fig. 17. Besides the LES data from [13], (isothermal) experimental results from [70] are also included, which were used in [13] as reference results as well. This already indicates that the velocity results are to be expected close to respective isothermal results. The results in Fig. 17 confirm this observation. Differences between the three methodical combinations are hardly visible, and the reference results are

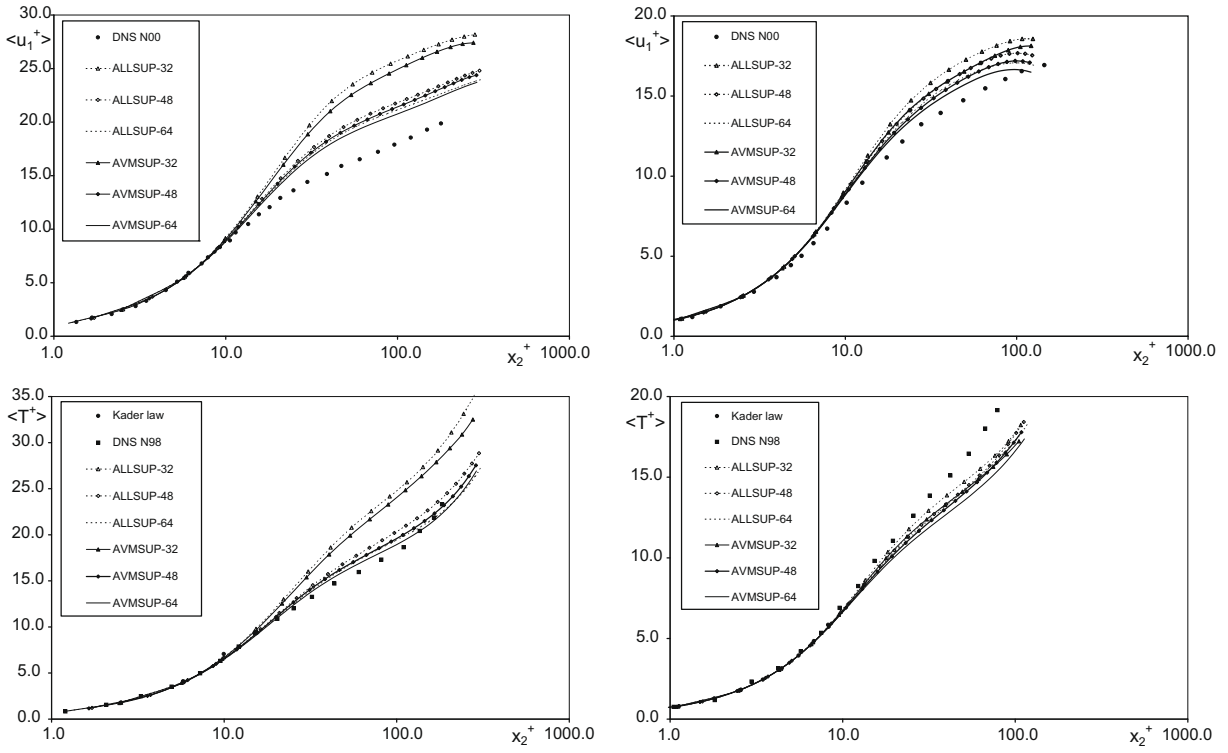

Fig. 12. Turbulent channel flow at temperature ratio $T_H/T_C = 2.00$ using AVMSUP and ALLSUP, top: mean streamwise velocity, bottom: mean temperature (left: lower channel half, right: upper channel half).

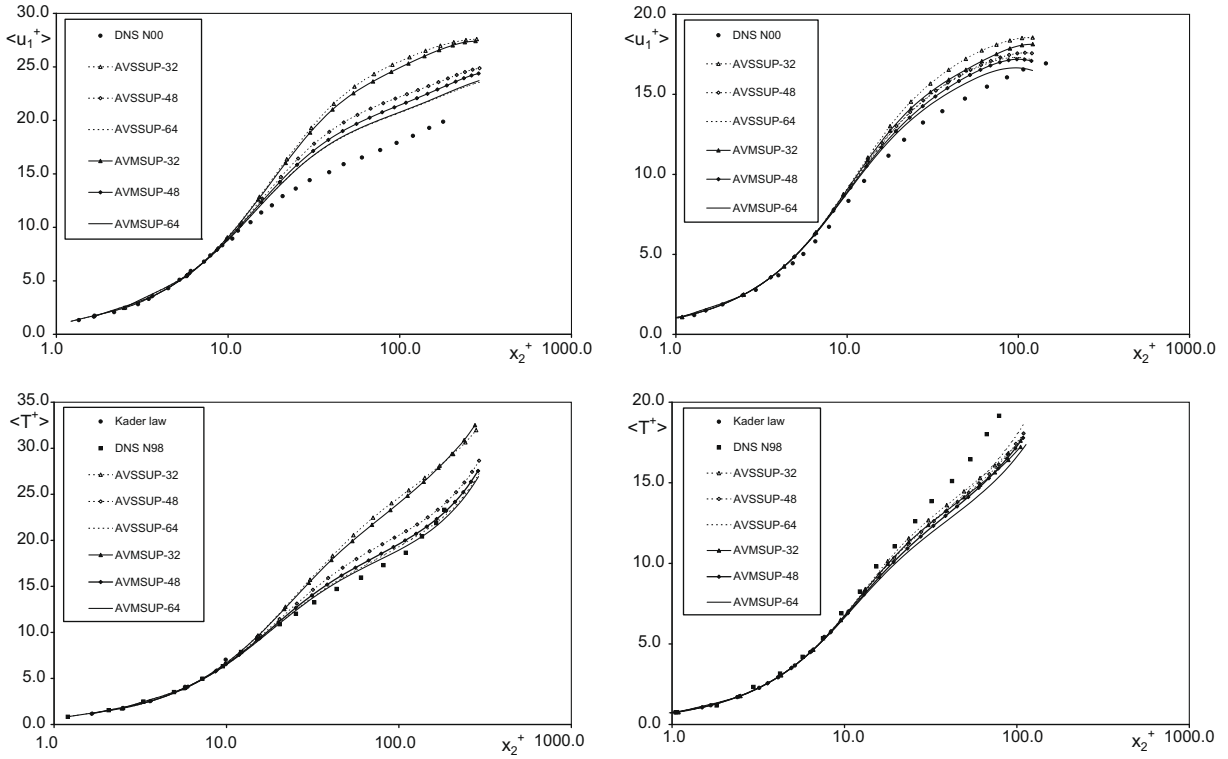

Fig. 13. Turbulent channel flow at temperature ratio $T_H/T_C = 2.00$ using AVMSUP and AVSSUP, top: mean streamwise velocity, bottom: mean temperature (left: lower channel half, right: upper channel half).

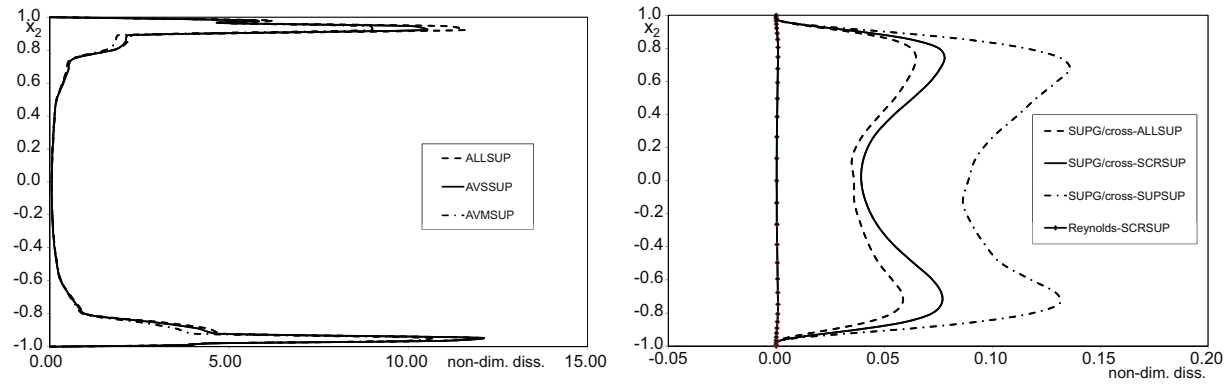

Fig. 14. Mean values of non-dimensionalized dissipation $\epsilon^{nd} = \epsilon h/(\rho_W u_\tau^3)$ for turbulent channel flow at temperature ratio $T_H/T_C = 1.01$ using various methods on a discretization with 32 finite elements in all spatial directions, left: dissipation due to small-scale subgrid-viscosity term, right: dissipation due to SUPG, cross- and Reynolds-stress terms.

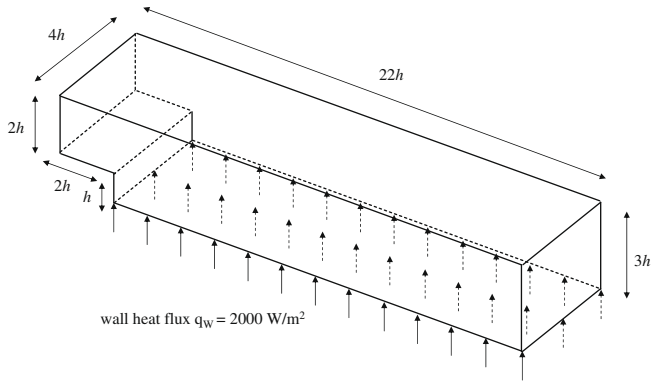

Fig. 15. Geometry of problem domain for backward-facing step.

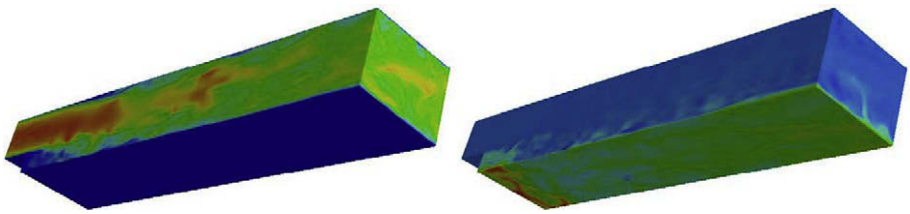

Fig. 16. Snapshots of velocity and temperature distributions at the beginning of the statistical period, left: colored velocity magnitude distribution, right: colored temperature distribution (red color indicates high velocity/temperature, blue color low velocity/temperature). (For interpretation of the references to colour in this figure legend, the reader is referred to the web version of this article.)

sufficiently well matched. At the first five locations, the present results are even somewhat closer to the experimental results than the LES AP02 data. Further downstream, the LES AP02 results are very close to the present ones.

Fig. 18 shows the temperature results at various locations after the step, scaled by the reference temperature and only for the region close to the bottom wall. As can be seen, the temperature values undergo substantial variations within small distances from the bottom wall. At about 0.02 m above the bottom wall, the reference temperature is almost reached again, but at the bottom wall, a maximum overheating of about up to 300% of the reference temperature is observed. The LES AP02 results at locations $x_1 = h$ and $x_1 = 3h$ are notably lower than the present ones and at locations $x_1 = 5h$, $x_1 = 7h$ and $x_1 = 9h$, they closely match. At the first location, $x_1 = h$, there is also a notable difference between the temperatures obtained with AVSSUP and the ones obtained with SUPSUP, SCRSUP as well as ALLSUP. Since, there are no other reference results in this context, we would like to oppose our results against the LES AP02. In particular, our suspicion is that the profile yielded by AVSSUP might be close to the actual temperature distribution. A DNS would probably clarify the actual temperature distribution in this region.

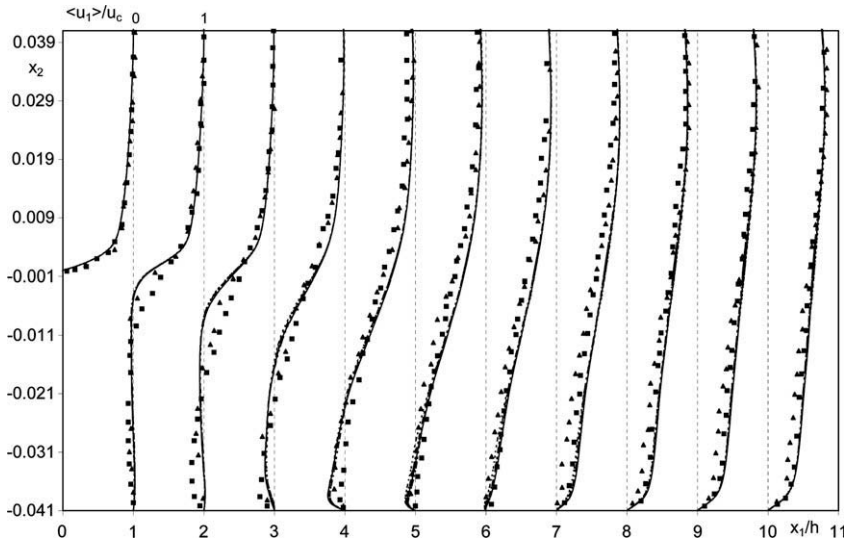

Fig. 17. Velocity results for backward-facing step, solid lines: AVSSUP, dashed lines: SCRSUP, dotted-dashed lines: ALLSUP, double-dotted-dashed lines: SUPSUP, squares: LES AP02, triangles: EXP KM95.

Our slight doubts with respect to the LES AP02 data in this region are based on the results for the skin-friction coefficient at the bottom wall, among other things. The skin-friction coefficient is defined as follows:

$$C_{\mathrm{f}}(x_1) = \frac{\langle \tau_{\mathrm{W}}^{h} \rangle (x_1)}{\frac{1}{2}\rho_{\mathrm{ref}} u_{1\mathrm{c}}^2}, \tag{28}$$

where

$$\tau_{\mathrm{W}} = \frac{\mu_{\mathrm{W}}}{\rho_{\mathrm{W}}} \frac{\partial u_{1\ \mathrm{W}}}{\partial x_2}. \tag{29}$$

The profiles for the skin-friction coefficient along the bottom wall are depicted in Fig. 19. As for the velocity results, differences between the various methodical combinations are minute. Surprisingly, the LES AP02 profile does not go to zero at the step wall, which is mandatory due to the presence of the (vertical) step wall and the resulting fact that the wall-shear stress needs to be zero at such a wall. For comparison, the DNS LMK97 data are also included in the diagram, with the profile in-

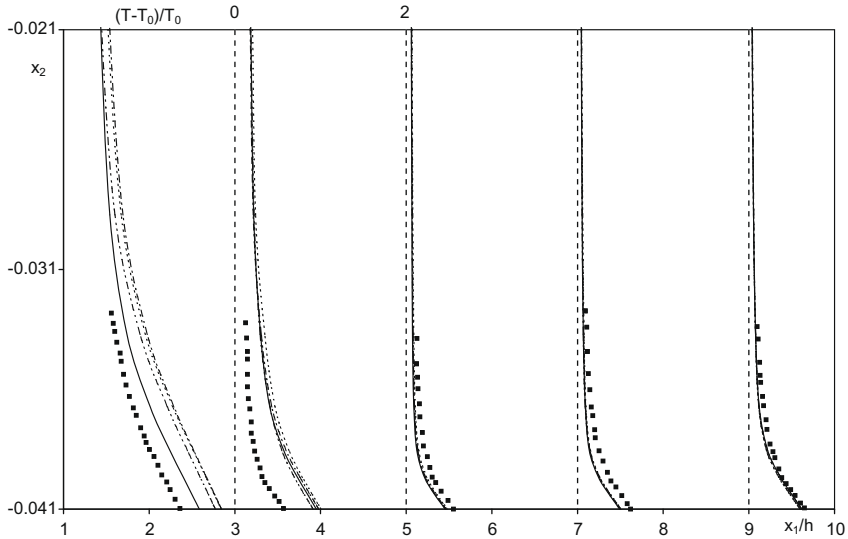

Fig. 18. Temperature results for backward-facing step, solid lines: AVSSUP, dashed lines: SCRSUP, dotted-dashed lines: ALLSUP, double-dotted-dashed lines: SUPSUP, squares: LES AP02.

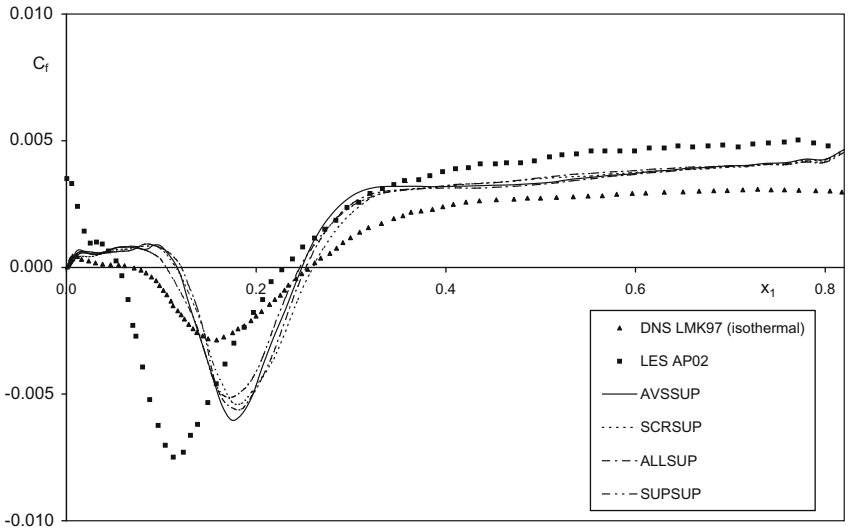

Fig. 19. Skin-friction coefficient at bottom wall of backward-facing step.

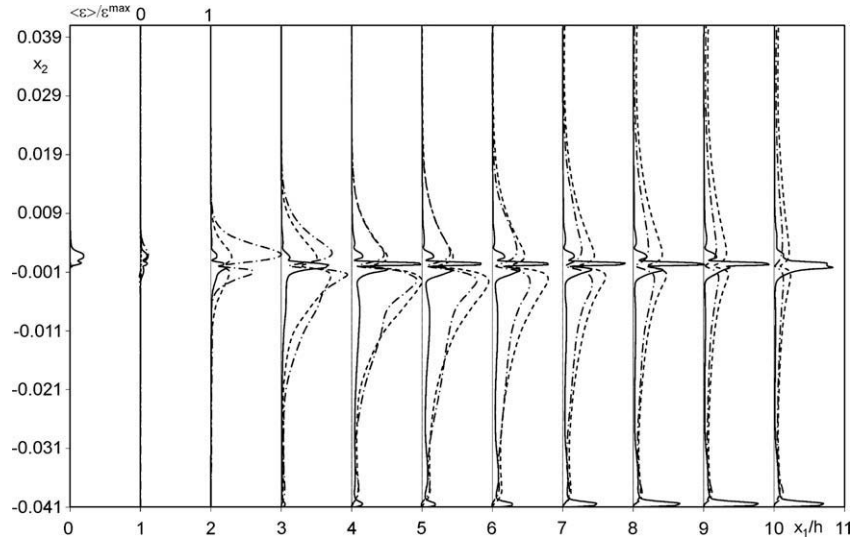

Fig. 20. Dissipation scaled by the respective maximum value for backward-facing step, solid lines: dissipation due to small-scale subgrid-viscosity term $\left(\epsilon_{ss}^{max} = 2.8 \times 10^{1}\right)$, dashed lines: dissipation due to SUPG/cross-stress term $\left(\epsilon_{SUPG/cross}^{max} = 7.2 \times 10^{-1}\right)$, dotted-dashed lines: dissipation due to Reynolds-stress term $\left(\epsilon_{Rey}^{max} = 7.5 \times 10^{-3}\right)$.

deed approaching zero at the step wall, as expected. The actual DNS LMK97 results are not comparable due to the fact that they originate from an isothermal investigation. Qualitatively, however, notably higher peak values for the skin-friction coefficient in the present case compared to an isothermal case are to be expected due to an increased ratio μ_W/ρ_W within the wall-shear stress τ_W, as observed in Fig. 19. Furthermore, the negative peak is somewhat shifted in downstream direction compared to the isothermal DNS LMK97.

As for the preceding numerical example, the dissipation introduced by various terms is analyzed using the measures as given in (24)–(27). The dissipation distributions due to small-scale subgrid-viscosity, SUPG/cross-stress and Reynolds-stress terms scaled by the respective maximum values are shown in Fig. 20. Two important observations can be made. First, the most pronounced dissipation values for all terms occur in the region around the (virtual) horizontal step line. For the small-scale subgrid-viscosity term, further notable peaks are observed in the vicinity of the lower walls. The peaks due to SUPG/cross-stress and Reynolds-stress dissipation in this area are less pronounced. Second, comparable to the channel, the maximum dissipation value due to the small-scale subgrid-viscosity term is about two orders of magnitude larger than the one due to the SUPG/cross-stress term, which is again about two orders of magnitude larger than the one due to the Reynolds-stress term.

7. Conclusions

An algebraic variational multiscale–multigrid method has been proposed for large-eddy simulation of turbulent variable-density flow at low Mach number. Scale-separating operators generated by level-transfer operators from plain aggregation algebraic multigrid methods enable the application of modeling terms to selected scale groups in a purely algebraic way. In the present context, this application of a modeling term is restricted to the smaller of the resolved problem scales. Following this purely algebraic strategy for scale separation means that no coarse discretization besides the basic one is required, in contrast to earlier approaches based on geometric multigrid methods. Plain aggregation algebraic multigrid is chosen in preference to smoothed aggregation algebraic multigrid because of the projective property inherent in a scale-separating operator based on the respective level-transfer operators. Among other things, this projective property enables an efficient implementation of the proposed method, as earlier demonstrated in [32,45].

This method, which was already successfully developed and applied for convection-dominated convection–diffusion problems in [31] and for large-eddy simulation of turbulent incompressible flow in [32,45], has been developed here for the considerably more demanding case of large-eddy simulation of turbulent variable-density flow at low Mach number. Furthermore, residual-based variational multiscale methods as originally proposed for turbulent incompressible flow in [29] and further evolved for variable-density flow at low-Mach number in [28] have also been subjected to a variety of such turbulent variable-density flow problems, and its results have been compared to the ones obtained with the algebraic variational multiscale–multigrid method.

Three numerical test cases of increasing complexity have been considered in this study: a Rayleigh–Taylor instability, turbulent channel flow with a heated and a cooled wall, and turbulent flow past a backward-facing step with heating. The first example, which represents a non-turbulent test problem with high density ratio, was chosen to evaluate the performance of the methods for such a problem configuration. In particular, it has been demonstrated that the small-scale subgrid-viscosity term, the essential part of the algebraic variational multiscale–multigrid method, does not deteriorate the results for such a non-turbulent problem configuration with high density ratio. On the contrary, an admittedly marginal and hardly notable improvement has been achieved compared to the residual-based method. This is in contrast to standard subgrid-viscosity models such as the (all-scale) Smagorinsky model with a constant coefficient, which are known to be over-dissipative in laminar and transitional situations, as outlined, e.g., in [4,71]. Hence, both the residual-based variational multiscale method and the algebraic variational multiscale–multigrid method investigated in this study are basically appropriate for simulations across all flow ranges, from laminar to turbulent.

In the second numerical example, turbulent channel flow with a heated and a cooled wall, the methods have been thoroughly evaluated via a refinement study employing three different meshes for two different temperature ratios. Mean and various second-order velocity and temperature results have indicated the higher prediction quality achievable when adding a small-scale subgrid-viscosity term within the algebraic multigrid framework instead of the residual-based terms accounting for the subgrid-scale part of the non-linear convective term. For several results, it has even been possible to counterbalance one mesh-refinement level via the addition of the small-scale subgrid-viscosity term. Finally, for turbulent flow past a backward-facing step with heating, the most complex test problem, similar velocity results have been obtained for both methods. However, the temperature results predicted by the algebraic variational multiscale–multigrid method have appeared to be closer to probable actual temperature profiles than the ones predicted by the residual-based method. A final judgement of this issue would require reliable DNS data for this case, though, which are not yet available.

During the course of the numerical evaluations, it has also been detected that the use of the small-scale subgrid-diffusivity term for the energy-conservation equation may rather jeopardize stability than improve the results. Also, the addition of cross- and Reynolds-stress terms for the energy-conservation equation eventually caused instabilities for turbulent flow over a backward-facing step with heating. Closer investigations specified their initial occurence within the lower-wall region where substantial temperature variations prevail; it seemed that rather the Reynolds- than the cross-stress term was responsible for the instabilities. For both turbulent channel flow with a heated and a cooled wall and turbulent flow past a backward-facing step with heating, the dissipation introduced by various subgrid-scale terms has been investigated. It has turned out for both problem configurations that the maximum dissipation values due to the small-scale subgrid-viscosity term are about two orders of magnitude larger than the ones due to the SUPG/cross-stress term, which are again about two orders of magnitude larger than the ones due to the Reynolds-stress term.

Acknowledgments

The support of the first author via the Emmy Noether Program of the Deutsche Forschungsgemeinschaft (DFG) is gratefully acknowledged.

References

[1] T.J.R. Hughes, L. Mazzei, K.E. Jansen, Large eddy simulation and the variational multiscale method, Comput. Visual. Sci. 3 (2000) 47–59.
[2] S.S. Collis, Monitoring unresolved scales in multiscale turbulence modeling, Phys. Fluids 13 (2001) 1800–1806.
[3] V. Gravemeier, The variational multiscale method for laminar and turbulent flow, Arch. Comput. Methods Eng. 13 (2006) 249–324.
[4] M. Germano, U. Piomelli, P. Moin, W.H. Cabot, A dynamic subgrid-scale eddy viscosity model, Phys. Fluids A 3 (1991) 1760–1765.
[5] J. Bardina, J.H. Ferziger, W.C. Reynolds, Improved subgrid scale models for large eddy simulation, AIAA Paper 80–1357, 1980.

[6] P. Sagaut, Large Eddy Simulation for Incompressible Flows, third ed., Springer-Verlag, Berlin, 2006.
[7] E. Garnier, N. Adams, P. Sagaut, Large Eddy Simulation for Compressible Flows, Scientific Computation, Springer, 2009.
[8] N. Peters, Turbulent Combustion, Cambridge University Press, Cambridge, 2000.
[9] R.S. Cant, E. Mastorakos, An Introduction to Turbulent Reacting Flows, Imperial College Press, London, 2008.
[10] A. Majda, J. Sethian, The derivation and numerical solution of the equations for zero Mach number combustion, Combust. Sci. Technol. 42 (1985) 185–205.
[11] W.P. Wang, R.H. Pletcher, On the large-eddy simulation of a turbulent channel flow with significant heat transfer, Phys. Fluids 8 (1996) 3354–3366.
[12] C. Pierce, P. Moin, Progress-variable approach for large eddy simulation of turbulent combustion, Report TF80, Flow Physics and Computation Division, Department of Mechanical Engineering, Stanford University, 2001.
[13] R.V.R. Avancha, R.H. Pletcher, Large eddy simulation of the turbulent flow past a backward-facing step with heat transfer and property variations, Int. J. Heat Fluid Flow 23 (2002) 601–614.
[14] B. Lessani, M.V. Paplexandris, Time-accurate calculation of variable density flows with strong temperature gradients and combustion, J. Comput. Phys. 212 (2006) 218–246.
[15] P. Wang, J. Fröhlich, V. Michelassi, W. Rodi, Large-eddy simulation of variable-density turbulent axisymmetric jets, Int. J. Heat Fluid Flow 29 (2008) 654–664.
[16] O. Desjardins, G. Blanquart, G. Balarac, H. Pitsch, High order conservative finite difference scheme for variable density low Mach number turbulent flows, J. Comput. Phys. 227 (2008) 7125–7159.
[17] P. Moin, K. Squires, W. Cabot, S. Lee, A dynamic subgrid-scale model for compressible turbulence and scalar transport, Phys. Fluids A 3 (1991) 2746–2757.
[18] G. Erlebacher, M.Y. Hussaini, C.G. Speziale, T.A. Zang, Toward the large-eddy simulation of compressible turbulent flows, J. Fluid Mech. 238 (1992) 155–185.
[19] M.P. Martin, U. Piomelli, G.V. Candler, Subgrid-scale models for compressible large-eddy simulations, Theoret. Comput. Fluid Dynam. 13 (2000) 361–376.
[20] V. Heuveline, On higher-order mixed FEM for low Mach number flows: applications to a natural convection benchmark problem, Int. J. Numer. Methods Fluids 41 (2003) 1339–1356.
[21] M.J. Martinez, D.K. Gartling, A finite element method for low-speed compressible flows, Comput. Methods Appl. Mech. Eng. 193 (2004) 1959–1979.
[22] A. Beccantini, E. Studer, S. Gournand, J.-P. Magnaud, T. Kloczko, C. Corre, S. Kudriakov, Numerical simulations of a transient injection flow at low Mach number regime, Int. J. Numer. Methods Eng. 76 (2008) 662–696.
[23] W. Liu, G. Makhviladze, An implict finite element solution of thermal flows at low Mach number, J. Comput. Phys. 227 (2008) 2743–2757.
[24] J. Principe, R. Codina, A stabilized finite element approximation of low speed thermally coupled flows, Int. J. Numer. Methods Heat Fluid Flow 18 (2008) 835–867.
[25] G. Hauke, L. Valiño, Computing reactive flows with a field Monte Carlo formulation and multi-scale methods, Comput. Methods Appl. Mech. Eng. 193 (2004) 1455–1470.
[26] J.N. Shadid, R.S. Tuminaro, K.D. Devine, G.L. Hennigan, P.T. Lin, Performance of fully coupled domain decomposition preconditioners for finite element transport/reaction simulations, J. Comput. Phys. 205 (2005) 24–47.
[27] M. Braack, T. Richter, Stabilized finite elements for 3-D reactive flows, Int. J. Numer. Methods Fluids 51 (2006) 981–999.
[28] V. Gravemeier, W.A. Wall, Residual-based variational multiscale methods for laminar, transitional and turbulent variable-density flow at low Mach number, Int. J. Numer. Methods Fluids, in press, available online: http://dx.doi.org/10.1002/fld.2242.
[29] Y. Bazilevs, V.M. Calo, J.A. Cottrell, T.J.R. Hughes, A. Reali, G. Scovazzi, Variational multiscale residual-based turbulence modeling for large eddy simulation of incompressible flows, Comput. Methods Appl. Mech. Eng. 197 (2007) 173–201.
[30] T.J.R. Hughes, G.R. Feijoo, L. Mazzei, J.-B. Quincy, The variational multiscale method – a paradigm for computational mechanics, Comput. Methods Appl. Mech. Eng. 166 (1998) 3–24.
[31] V. Gravemeier, M.W. Gee, W.A. Wall, An algebraic variational multiscale–multigrid method based on plain aggregation for convection–diffusion problems, Comput. Methods Appl. Mech. Eng. 198 (2009) 3821–3835.
[32] V. Gravemeier, M.W. Gee, M. Kronbichler, W.A. Wall, An algebraic variational multiscale–multigrid method for large eddy simulation of turbulent flow, Comput. Methods Appl. Mech. Eng. 199 (2010) 853–864.
[33] P.T. Lin, M. Sala, J.N. Shadid, R.S. Tuminaro, Performance of fully coupled algebraic multilevel domain decomposition preconditioners for incompressible flow and transport, Int. J. Numer. Methods Eng. 67 (2006) 208–225.
[34] M.-H. Lallemand, H. Steve, A. Dervieux, Unstructured multigridding by volume agglomeration: current status, Comput. Fluids 21 (1992) 397–433.
[35] D.J. Mavriplis, V. Venkatakrishnan, A 3D agglomeration multigrid solver for the Reynolds-averaged Navier–Stokes equations on unstructured meshes, Int. J. Numer. Methods Fluids 23 (1996) 527–544.
[36] B. Koobus, C. Farhat, A variational multiscale method for the large eddy simulation of compressible turbulent flows on unstructured meshes – application to vortex shedding, Comput. Methods Appl. Mech. Eng. 193 (2004) 1367–1383.
[37] P.R. Voke, Multiple mesh simulation of low Reynolds number turbulent channel flow, in: C. Taylor, R. Sani (Eds.), Numerical Methods in Laminar and Turbulent Flow, vol. 6, 1989, pp. 1567–1577.
[38] M. Terracol, P. Sagaut, C. Basdevant, A multilevel algorithm for large-eddy simulation of turbulent compressible flows, J. Comput. Phys. 167 (2001) 439–474.
[39] P. Sagaut, S. Deck, M. Terracol, Multiscale and Multiresolution Approaches in Turbulence, Imperial College Press, London, 2006.
[40] V. Gravemeier, Scale-separating operators for variational multiscale large eddy simulation of turbulent flows, J. Comput. Phys. 212 (2006) 400–435.
[41] T.J.R. Hughes, G.N. Wells, Conservation properties for the Galerkin and stabilised forms of the advection–diffusion and incompressible Navier–Stokes equations, Comput. Methods Appl. Mech. Eng. 194 (2005) 1141–1159.
[42] A.N. Brooks, T.J.R. Hughes, Streamline Upwind/Petrov–Galerkin formulations for convection dominated flows with particular emphasis on the incompressible Navier–Stokes equations, Comput. Methods Appl. Mech. Eng. 32 (1982) 199–259.
[43] T.J.R. Hughes, The Finite Element Method: Linear Static and Dynamic Finite Element Analysis, Prentice-Hall, Englewood Cliffs, NJ, 1987.
[44] K.E. Jansen, C.H. Whiting, G.M. Hulbert, A generalized-α method for integrating the filtered Navier–Stokes equations with a stabilized finite element method, Comput. Methods Appl. Mech. Eng. 190 (2000) 305–319.
[45] V. Gravemeier, M. Kronbichler, M.W. Gee, W.A. Wall, An algebraic variational multiscale–multigrid method for large eddy simulation: generalized-α time integration, Fourier analysis and application to turbulent flow past a square-section cylinder, Comput. Mech., preprint, submitted for publication.
[46] J. Smagorinsky, General circulation experiments with the primitive equations. I. The basic experiment, Mon. Weather Rev. 91 (1963) 99–164.
[47] J.W. Deardorff, A numerical study of three-dimensional turbulent channel flow at large Reynolds numbers, J. Fluid Mech. 41 (1970) 453–465.
[48] H. Kawamura, K. Ohsaka, H. Abe, K. Yamamoto, DNS of turbulent heat transfer in channel flow with low to medium-high Prandtl number fluid, Int. J. Heat Fluid Flow 19 (1998) 482–491.
[49] J.-L. Guermond, Stabilization of Galerkin approximations of transport equations by subgrid modeling, Math. Model. Numer. Anal. 33 (1999) 1293–1316.
[50] P. Vaněk, J. Mandel, M. Brezina, Algebraic multigrid based on smoothed aggregation for second and fourth order problems, Computing 56 (1996) 179–196.
[51] R.R. Nourgaliev, T.G. Theofanous, High-fidelity interface tracking in compressible flows: unlimited anchored adaptive level set, J. Comput. Phys. 224 (2007) 836–866.
[52] F. Nicoud, Numerical study of a channel flow with variable properties, in: Annual Research Briefs – 1998, Center for Turbulence Research, Stanford University and NASA Ames Research Center, 1998, pp. 289–310.

[53] F. Nicoud, Conservative high-order finite difference schemes for low-Mach number flows, J. Comput. Phys. 158 (2000) 71–97.
[54] B. Debusschere, C.J. Rutland, Turbulent scalar transport mechanisms in plane channel and Couette flows, Int. J. Heat Mass Transfer 47 (2004) 1771.
[55] R.D. Moser, J. Kim, N.N. Mansour, Direct numerical simulation of turbulent channel flow up to $Re_\tau = 590$, Phys. Fluids 11 (1999) 943–945.
[56] S. Suslov, S. Paolucci, Stability of mixed-convection flow in a tall vertical channel under no-Boussinesq conditions, J. Fluid Mech. 302 (1995) 91–115.
[57] A.V. Trofimova, A.E. Tejada-Martinez, K.E. Jansen, R.T. Lahey Jr., Direct numerical simulation of turbulent channel flows using a stabilized finite element method, Comput. Fluids 38 (2009) 924–938.
[58] Z. Wang, A.A. Oberai, Spectral analysis of the dissipation of the residual-based variational multiscale method, Comput. Methods Appl. Mech. Eng. 199 (2010) 810–818.
[59] A.E. Tejada-Martínez, K.E. Jansen, On the interaction between dynamic model dissipation and numerical dissipation due to streamline upwind/Petrov–Galerkin stabilization, Comput. Methods Appl. Mech. Eng. 194 (2005) 1225–1248.
[60] J.C. Vogel, J.K. Eaton, Combined heat transfer and fluid dynamic measurements downstream of a backward facing step, J. Heat Transfer 107 (1985) 922–929.
[61] O. Labbe, P. Sagaut, E. Montreuil, Large-eddy simulation of heat transfer over a backward-facing step, Numer. Heat Transf. A-Appl. 42 (2002) 73–90.
[62] A. Keating, U. Piomelli, K. Bremhorst, C. Nesic, Large-eddy simulation of heat transfer downstream of a backward-facing step, J. Turbul. 5 (2004) 020.
[63] D. You, P. Moin, A dynamic global-coefficient subgrid-scale model for large-eddy simulation of turbulent scalar transport in complex geometries, Phys. Fluids 21 (2009). 045109-1–045109-10.
[64] H. Le, P. Moin, J. Kim, Direct numerical simulation of turbulent flow over a backward-facing step, J. Fluid Mech. 330 (1997) 349–374.
[65] R. Friedrich, M. Arnal, Analysing turbulent backward-facing step flow with the lowpass-filtered Navier–Stokes equations, J. Wind Eng. Ind. Aerodyn. 35 (1990) 101–128.
[66] Y. Bazilevs, C. Michler, V.M. Calo, T.J.R. Hughes, Isogeometric variational multiscale modeling of wall-bounded turbulent flows with weakly-enforced boundary conditions on unstretched meshes, Comput. Methods Appl. Mech. Eng. 199 (2010) 780–790.
[67] T.S. Lund, X. Wu, K.D. Squires, Generation of turbulent inflow data for spatially-developing boundary layer simulations, J. Comput. Phys. 140 (1998) 233–258.
[68] M. Pamies, P.-E. Weiss, E. Garnier, S. Deck, P. Sagaut, Generation of synthetic turbulent inflow data for large eddy simulation of spatially evolving wall-bounded flows, Phys. Fluids 21 (2009). 045103-1–045103-15.
[69] K. Akselvoll, P. Moin, Large eddy simulation of turbulent confined coannular jets and turbulent flow over a backward-facing step, Report TF63, Department of Mechanical Engineering, Stanford University, 1995.
[70] N. Kasagi, A. Matsunaga, Three-dimensional particle-tracking velocimetry measurement of turbulence statistics and energy budget in a backward-facing step flow, Int. J. Heat Fluid Flow 16 (1995) 477–485.
[71] C. Meneveau, J. Katz, Scale-invariance and turbulence models for large-eddy simulation, Ann. Rev. Fluid Mech. 32 (2000) 1–32.